HHS Public Access

Author manuscript

*Nat Biomed Eng*. Author manuscript; available in PMC 2019 April 03.

Published in final edited form as:

*Nat Biomed Eng*. 2018 May ; 2(5): 279–292. doi:10.1038/s41551-018-0221-2.

# Efficacy and safety assessment of a TRAF6-targeted nanoimmunotherapy in atherosclerotic mice and non-human primates

**Marnix Lameijer**[1,2], **Tina Binderup**[3], **Mandy M.T. van Leent**[1,2], **Max L. Senders**[1,2], **Francois Fay**[1], **Joost Malkus**[1], **Brenda L. Sanchez-Gaytan**[1], **Abraham J. P. Teunissen**[1], **Nicolas Karakatsanis**[1], **Philip Robson**[1], **Xianxiao Zhou**[4], **Yuxiang Ye**[5], **Gregory Wojtkiewicz**[5], **Jun Tang**[6], **Tom T.P. Seijkens**[2], **Jeffrey Kroon**[7], **Erik S.G. Stroes**[7], **Andreas Kjaer**[3], **Jordi Ochando**[8], **Thomas Reiner**[6], **Carlos Pérez-Medina**[1], **Claudia Calcagno**[1], **Edward A. Fischer**[9], **Bin Zhang**[4], **Ryan E. Temel**[10], **Filip K. Swirski**[5], **Matthias Nahrendorf**[5], **Zahi A. Fayad**[1], **Esther Lutgens**[2,11], **Willem J.M. Mulder**[1,2], and **Raphaël Duivenvoorden**[1,7,12]

[1]Translational and Molecular Imaging Institute, Icahn School of Medicine at Mount Sinai, New York, NY, USA. [2]Department of Medical Biochemistry, Academic Medical Center, Amsterdam, The Netherlands. [3]Cluster for molecular Imaging and Department of Clinical Physiology, Nuclear Medicine & PET, Rigshospitalet and University of Copenhagen, Copenhagen, Denmark. [4]Department of Genetics and Genomic Sciences, Icahn School of Medicine at Mount Sinai, New York, NY, USA. [5]Center for Systems Biology, Massachusetts General Hospital, and Division of Cardiovascular Medicine, Brigham and Women's Hospital, Harvard Medical School, Boston, MA. [6]Department of Radiology, Memorial Sloan Kettering Cancer Center, 1275 York Avenue, New York, NY 10065. [7]Department of Vascular Medicine, Amsterdam Cardiovascular Sciences, Academic Medical Center, Amsterdam, The Netherlands. [8]Immunology Institute, Department of Oncological Sciences, Icahn School of Medicine at Mount Sinai, New York, NY, USA. [9]Department of Medicine (Cardiology) and Cell Biology, Marc and Ruti Bell Program in Vascular



**Corresponding Authors:** Raphaël Duivenvoorden; r.duivenvoorden@amc.uva.nl, Department of Vascular Medicine, Amsterdam Cardiovascular Sciences, Department of Nephrology, Academic Medical Center, Amsterdam, The Netherlands. Meibergdreef 9, 1105 AZ Amsterdam-Zuidoost. Tel: +31 20 566 5157, Willem J.M. Mulder; willem.mulder@mssm.edu, Translational and Molecular Imaging Institute, Icahn School of Medicine at Mount Sinai, New York, NY, USA. 1470 Madison Avenue, NY 10029. Tel: +1 (212) 824-8471.

Author contributions

R.D. and W.J.M.M. designed the study. R.D., M.L, T.B., M.M.T.v.L., M.L.S., J.T., T.T.P.S., J.K., E.S.G.S., J.O., E.A.F., R.E.T., N.K, P.R., A.K., F.K.S., M.N., Z.A.F., E.L., W.J.M.M. designed, performed and oversaw in vivo and ex vivo experiments. F.F., B.L.S-G and M.L developed and produced TRAF6i-HDL. Flow cytometry, histology and immunostaining, laser capture microdissection, blood chemistry were performed and analyzed by R.D., M.L., M.M.T.v.L., J.M. FMT-CT was performed and analyzed by R.D., Y.Y., G.W, and M.N. The RNAseq was performed and analyzed by X.Z., B.Z., R.D., M.L. Monocyte migration assay was performed by J.K. PET-CT and pharmacokinetics studies in mice were performed by C.P.M, J.T., and T.R. $^{89}$Zr-PET/MRI in non-human primates was performed and analyzed by T.B., M.L.S., C.P.M, C.C. The manuscript was written by R.D., M.L. and W.J.M.M. All authors contributed to writing the manuscript and approved the final draft. R.D., Z.A.F. and W.J.M.M. provided funding.

Data Availability

The authors declare that all data supporting the findings of this study are available within the paper and its supplementary information. RNA sequencing data is available at the Gene Expression Omnibus (GEO) database (GEO series number GSE104777, https://www.ncbi.nlm.nih.gov/geo/).

Competing interests

There authors declare no competing financial interests.

Biology, NYU School of Medicine, New York, USA. [10]Saha Cardiovascular Research Center & Department of Pharmacology and Nutritional Sciences, University of Kentucky, Lexington, KY, USA. [11]Institute for Cardiovascular Prevention, Ludwig Maximilian's University, Munich, Germany [12]Department of Nephrology, Academic Medical Center, Amsterdam, The Netherlands.

## Abstract

In atherosclerosis, macrophage accumulation is directly linked to the destabilization and rupture of plaque, causing acute atherothrombotic events. Circulating monocytes enter the plaque and differentiate into macrophages, where they are activated by CD4+ T-lymphocytes through CD40-CD40 ligand signalling. Here, we report the development and multiparametric evaluation of a nanoimmunotherapy that moderates CD40-CD40 ligand signalling in monocytes and macrophages by blocking the interaction between CD40 and tumour necrosis factor receptor-associated factor 6 (TRAF6). We evaluated the biodistribution characteristics of the nanoimmunotherapy in Apolipoprotein E deficient (Apoe−/−) mice and in non-human primates by in vivo PET imaging. In Apoe−/− mice, a one-week nanoimmunotherapy treatment regimen achieved significant anti-inflammatory effects, caused by the impaired migration capacity of monocytes, as established by transcriptome analysis. The rapid reduction of plaque inflammation by the TRAF6-targeted nanoimmunotherapy and its favourable toxicity profiles in both mice and non-human primates highlights the translational potential of this strategy for the treatment of atherosclerosis.

## Introduction

The recruitment of monocytes to the vessel wall is a key contributing process to macrophage accumulation in the atherosclerotic plaque[1]. This process is directly linked to the development of atherothrombotic events[1].

As early as in the 1990s, it was recognized that the activation of plaque monocytes and macrophages by CD4+ T-lymphocytes via CD40-CD40 ligand (CD40-CD40L) signaling plays a central role in abetting plaque inflammation[2], paving the way for new immunotherapeutic avenues[3-6]. Subsequent studies revealed that tumor necrosis factor receptor-associated factor 6 (TRAF6) is of specific importance in propelling CD40's signaling cascade inside monocytes and macrophages[7]. Deficiency of CD40-TRAF6 interactions in myeloid cells has been shown to decrease monocyte recruitment to plaques and abolish atherosclerotic plaque formation in Apoe−/− mice[7].

This study's goal was to develop and multiparametrically evaluate a targeted nanoimmunotherapy that specifically blocks the CD40-TRAF6 interaction in monocytes and macrophages. For this purpose, we incorporated a recently developed small molecule inhibitor of the CD40-TRAF6 interaction in reconstituted HDL (TRAF6i-HDL)[8,9]. We show in an Apoe−/− mouse model of atherosclerosis that TRAF6i-HDL is taken up by monocytes and macrophages, while lymphocytes do not take up the nanoimmunotherapy. Fully integrated three-dimensional positron emission tomography with magnetic resonance imaging (PET/MRI) methods were developed to non-invasively study TRAF6i-HDL's pharmacokinetics and biodistribution in non-human primates. Therapeutic studies in

atherosclerotic mice revealed TRAF6i-HDL nanoimmunotherapy's ability to rapidly decrease monocyte recruitment, thereby decreasing plaque inflammation. In line with these findings, whole transcriptome analysis and an in vitro assay indicated that cell migration was among the affected cellular processes. Finally, TRAF6i-HDL's safety was established in both atherosclerotic mice and non-human primates (NHPs).

## Results

### TRAF6i-HDL characteristics.

This study's aim was to decrease plaque inflammation by moderating CD40-CD40 ligand signalling in monocytes and macrophages via site-specific blocking of the interaction between CD40 and TRAF6. (TRAF6i-HDL, schematically shown in Fig. 1a). TRAF6i-HDL was constructed from human apolipoprotein A-I (apoA-I), and the phospholipids 1-myristoyl-2-hydroxy-sn-glycero-phosphocholine (MHPC) and 1,2-dimyristoyl-sn-glycero-3-phosphatidylcholine (DMPC), in which a lipophilic small molecule inhibitor (SMI 6877002) of CD40-TRAF6 interaction was encapsulated[8]. SMI 6877002 binds to the TRAF6 binding site on CD40 and not to the TRAF6 bindings sites on the IRAKs, leaving IL-1R/TLR signaling unaffected[8]. The mean size and polydisperisty, as determined by dynamic light scattering, of the different TRAF6i-HDL batches used in this study were 20.7 ± 3.0 nm and 0.26 ± 0.07 (n=10 batches), respectively. Transmission electron micrographs are shown in Supplementary Fig. 1. TRAF6i-HDL variants, incorporating fluorescent dyes (DiO or DiR) or Zirconium-89 ($^{89}$Zr) radiolabeled phospholipids, were synthesized to allow their detection by fluorescence techniques, positron emission tomography (PET), gamma counting and autoradiography. Additional data on nanoparticle characteristics, such as stability, drug release and labeling, are provided in Supplementary fig. 2.

### Study outline.

A schematic overview of the study design is shown in Fig. 1b. First, we studied TRAF6i-HDL's pharmacokinetics, biodistribution, and atherosclerotic plaque monocyte and macrophage targeting efficiency in atherosclerotic mice. In parallel, we developed an in vivo positron emission tomography with magnetic resonance (PET/MRI) protocol to longitudinally study TRAF6i-HDL's biodistribution in non-human primates. Subsequently, in atherosclerotic mice, plaque regression efficacy of a one-week TRAF6i-HDL regimen involving four intravenous infusions was studied by immunohistochemistry. TRAF6i-HDL's effects on the immune system were studied as well. To shed light on the therapeutic mechanism, whole transcriptome analysis of plaque macrophages, in vitro transendothelial migration assays, and in vivo imaging of protease activity in the aortic sinus area was performed. Finally, the TRAF6i-HDL nanoimmunotherapy's safety was established in atherosclerotic mice and non-human primates.

### Pharmacokinetics and biodistribution studies in Apoe−/− mice.

To investigate its pharmacokinetics and biodistribution, Apoe−/− mice received a single infusion of Zirconium-89-radiolabeled TRAF6i-HDL ($^{89}$Zr-TRAF6i-HDL). Blood radioactivity clearance of $^{89}$Zr-TRAF6i-HDL was measured over 24 hours and data were fitted using a two-phase decay non-linear regression. The weighted blood half-life (t½) was

finally calculated to be 124.4 minutes based on a t½-fast of 13.7 minutes and a t½-slow of 195 minutes (Fig. 1c).

Biodistribution was evaluated by in vivo positron emission tomography with computed tomography (PET/CT) imaging (Fig. 1d) and validated by ex vivo gamma counting, the latter expressed as a percentage of injected dose per gram tissue (%ID/g; Fig. 1e). As expected, PET/CT imaging showed that $^{89}$Zr-TRAF6i-HDL primarily accumulated in the liver, spleen and kidneys, organs known to take up and metabolize HDL. Gamma counting data confirmed these results, showing $^{89}$Zr-TRAF6i-HDL uptake of 12.8 %ID/g in the liver, 8.9 %ID/g in the spleen, and 7.9 %ID/g in the kidneys. In comparison, the heart, a similar sized organ, only contained 1.1 %ID/g (Fig. 1e). Ex vivo near infrared fluorescence (NIRF) imaging, 24 hours after infusion, corroborated the PET/CT and gamma counting observations, showing that TRAF6i-HDL accumulates primarily in the liver, spleen and kidneys (Fig. 1f).

Flow cytometry analyses revealed that Ly6C$^{hi}$ monocytes and macrophages in blood, bone marrow, and spleen took up DiO core labeled TRAF6i-HDL. Neutrophils, Ly6C$^{lo}$ monocytes and dendritic cells also took up DiO-TRAF6i-HDL, while lineage positive CD11b negative cells (all non-myeloid cells) did not (Supplementary Fig. 3), indicative of myeloid cell specificity.

### TRAF6i-HDL accumulation in atherosclerotic lesions.

Ex vivo gamma counting of whole aortas showed that 1.3% ID/g of $^{89}$Zr-TRAF6i-HDL had accumulated 24 hours after infusion (Fig. 1e). Looking specifically at $^{89}$Zr-TRAF6i-HDL distribution throughout the aorta, the uptake was highest in the aortic sinus area (Fig. 1g), which is the preferential site of plaque development in this mouse model. While only accounting for 6.4% of the total area, the aortic sinus area generated approximately 29% of the signal, corresponding to 5.9 %ID/g (Fig 1d). NIRF imaging showed similar preferential accumulation of DiR-labeled TRAF6i-HDL in the aortic sinus area (Fig. 1h).

Cell specificity of DiO labeled TRAF6i-HDL uptake in aortic plaque was assessed by flow cytometry. We found that 86% of macrophages and 81% of Ly6C$^{hi}$ monocytes had taken up DiO-TRAF6i-HDL, while lineage positive cells (all non-myeloid cells) had taken up virtually none (Fig. 1i). Furthermore, the majority of neutrophils (64%) and dendritic cells (61%) in the aortic plaque were found to contain DiO-TRAF6i-HDL (Supplementary Fig. 3). These results mirror our findings in blood, bone marrow and spleen, showing that cells of the myeloid lineage, and in particular the Ly6C$^{hi}$ monocyte subset and macrophages show a high uptake of TRAF6i-HDL nanoparticles.

### PET/MRI-facilitated pharmacokinetics and biodistribution studies in non-human primates.

To assess biodistribution in non-human primates, we developed a fully integrated three-dimensional PET/MR protocol that allows dynamic and longitudinal imaging of $^{89}$Zr-TRAF6i-HDL. Six non-human primates were subjected to full body PET/MR imaging (See Supplementary movie 1 for three-dimensional rendered MRI data) after intravenous administration of $^{89}$Zr-TRAF6i-HDL. The animals were dynamically imaged over the course of the first hour post administration, while subsequent static scans were performed at

1, 24, 48 and 72 hours. Dynamic PET imaging showed rapid radioactivity accumulation in the liver, spleen and kidneys, followed by a significant uptake in the bone marrow (Fig. 2a, Supplementary movie 2). One hour post injection, PET images revealed a strong kidney $^{89}$Zr-TRAF6i-HDL signal, followed by the liver and spleen (Fig. 2a). At 24, 48 and 72 hours, radioactivity was found accumulated mostly in the liver and spleen (Fig. 2b). After sacrificing the animals at the 72 hour time point, tissue gamma counting showed that the largest amount of the injected dose (%ID/g) could be traced back to the liver and spleen, followed by the kidneys, corroborating the in vivo PET/MRI findings (Fig. 2c, Supplementary Fig. 4a and 4b). Blood was collected at different time points and the data were fitted using a two-phase decay non-linear regression. The t½-fast was 14.2 minutes and the t½-slow was 513 minutes, resulting in a weighted blood half-life (t½) of 272 minutes (Fig. 2d).

### In vivo effects of TRAF6i-HDL on plaque inflammation.

To assess TRAF6i-HDL's therapeutic efficacy, we used 20 week old Apoe−/− mice that had been on a high-cholesterol diet for 12 weeks in order to develop atherosclerotic lesions. While all mice remained on a high-cholesterol diet, they received four intravenous infusions of control PBS, control HDL nanoparticles, or TRAF6i-HDL over a period of 7 days. The CD40-TRAF6 inhibitor dose administered per infusion was 5 mg/kg. To limit a concomitant therapeutic effect of apoA-I itself, we used a low apoA-I dose of 9 mg/kg. All mice were sacrificed 24 hours after the final infusion.

For the first experiment, we performed quantitative histologic analysis of plaques in the aortic sinus area in mice treated with control, HDL or TRAF6i-HDL (n=10 per group). Cross-sections were stained with Hematoxylin and Eosin (H&E) and Sirius Red (collagen), and immunostained for Mac3 (macrophages) and Ki67 (proliferating cells). No significant difference in plaque size or collagen content was observed across the groups (Fig. 3a). However, in TRAF6i-HDL-treated mice, the percentage of Mac3 positive area was markedly decreased by 36% ($p=0.001$) and 37% ($p<0.001$) as compared to the control and HDL groups, respectively (Fig. 3b). As a result, the Mac3 to collagen ratio in the plaque was favorably affected towards a more stable plaque phenotype in the TRAF6i-HDL group, as the ratio was decreased by 31% ($p<0.001$) and 36% ($p=0.004$) compared to the control and HDL groups (Fig. 3b). The number of proliferating macrophages was similar in all groups (Fig. 3a), indicating that the observed decrease in plaque macrophages was not caused by a decrease in local proliferation of macrophages. Previous studies showed that in addition to monocyte recruitment, local macrophage proliferation plays a pivotal role in fueling plaque inflammation[10].

Next, we focused on quantification of aorta macrophage content by flow cytometry of whole aortas. Again, 20 week old Apoe−/− mice on a high-cholesterol diet were treated with either control (n=27), HDL (n=27) or TRAF6i-HDL (n=27). Aorta macrophage content decreased markedly in the TRAF6i-HDL treated group, by 66% and 67% ($p<0.001$ for both comparisons), as compared to the control and HDL groups (Fig. 4a). Furthermore, in the TRAF6i-HDL treated group, aorta T-lymphocyte content was decreased by 65% and 49% when compared to controls and HDL, respectively (Supplementary Fig. 5). Altogether these

data indicate a potent anti-inflammatory effect of TRAF6i-HDL in atherosclerotic plaques after only a single week of therapy.

Since we had already observed that the number of proliferating Ki67+ macrophages was not affected by therapy, we hypothesized that the decrease in plaque macrophages content and inflammation is caused by decreased monocyte recruitment instead[11,12]. To further investigate this, we first quantified aortic Ly6C$^{hi}$ monocytes in the same flow cytometry experiment as the one in which we measured macrophage content. We observed that the decrease in macrophages was paralleled by a 49% and 52% ($p<0.001$ for both comparisons) decrease in Ly6C$^{hi}$ monocytes in the aorta, as compared to the control and HDL groups, respectively (Fig. 4a). Interestingly, the reduction in aortic Ly6C$^{hi}$ monocyte content could not be explained by a systemic decrease in Ly6C$^{hi}$ monocytes (Fig. 4b). Instead, we observed an increase in the percentage of Ly6C$^{hi}$ monocytes in the bone marrow, spleen and blood. The cause of the relative increase is not entirely clear. Enhanced monocyte survival is unlikely to be the cause, since stimulation of CD40 signaling is known to enhance monocyte survival, while we inhibited the CD40 signaling pathway.[13] Increased monocyte production in the bone marrow and/or decreased migration into the peripheral tissues perhaps may play a role, however this cannot be concluded solely based on this experiment.

Secondly, we performed an experiment in which the thymidine analogue 5- bromo-2'-deoxyuridine (BrdU) was injected intraperitoneally 2 hours prior to sacrificing the mice. BrdU incorporates into newly synthesized DNA, and therefore can be used as a marker for proliferation. Fig. 4c shows that the percentage of plaque macrophages that had incorporated BrdU was not decreased by TRAF6i-HDL therapy. This result is in line with the histology observation on Ki67 expression. In an in vitro experiment with RAW 264.7 cell line of murine macrophages, characterized by a high proliferation rate[14], incubation with the CD40-TRAF6 inhibiting compound or TRAF6i-HDL did not decrease the proliferation rate (Fig. 4d).

Taken together, these data indicate that plaque macrophage content was decreased by TRAF6i-HDL therapy. The mechanism by which TRAF6i-HDL decreases plaque inflammation is likely mediated through the abatement of monocyte recruitment, while local macrophage proliferation is not affected.

### TRAF6i-HDL's mechanism of action.

In order to gain insight into the effects of TRAF6i-HDL on gene expression of plaque monocytes / macrophages, we isolated CD68 positive cells from aortic sinus plaques by laser capture microdissection of mice either treated with control or TRAF6i-HDL. Whole RNA of these cells was isolated for sequencing. We identified genes that were differentially expressed (DE) between control and TRAF6i-HDL treated mice. Correction for multiple testing was performed with a false discovery rate (FDR) < 0.2 (Fig. 5a). A total of 416 DE genes were identified, of which 209 genes were down-regulated and 207 up-regulated (Fig. 5b). Gene ontology (GO)-function was used to annotate the DE genes, and to find cellular components that significantly enriched with DE genes (Fig. 5c). In the 15 enriched GO terms that significantly enriched with DE genes, "focal adhesion" is of most interest. Other enriched GO terms, such as "cell-substrate adherent junction", "cell-substrate junction",

"adherence junction", and "anchoring junction" are closely related to "focal adhesion" and the genes in these GO terms overlapped to a high degree (Supplementary Table 1). Focal adhesion is a dynamic process in which protein complexes connect to the extracellular matrix, and plays a central role in monocyte and macrophage migration[15]. In a subsequent analysis, the same 416 DE genes were mapped with the Kyoto Encyclopedia of Genes and Genomes (KEGG) pathway tool, by which we identified two significantly altered pathways, namely "focal adhesion" and "endocytosis" (Fig. 5d, Supplementary Table 2). DE genes in the "focal adhesion" pathway of specific interest are Rhoa, Rap1a and Rap1b, which play a central role in the regulation of monocyte migration by activating integrins[14]. They were all significantly down-regulated. One of the most highly up-regulated DE genes (FDR < 0.05) was Stab1 (encodes for Stabilin-1), which is associated with an atheroprotective macrophage phenotype and is known to have functions in lymphocyte homing and cell adhesion[16,17]. Also other highly significant DE genes (FDR < 0.05) were identified that are not known to be related to monocyte migration (Fig. 5d, Supplementary Table 3). We did not observe an effect on gene expression related to macrophage proliferation, apoptosis, migratory egress, macrophage polarization, or monocyte to macrophage differentiation (Supplementary Table 4). These data are in line with our in vivo observations of decreased Ly6C$^{hi}$ monocyte recruitment in TRAF6i-HDL treated Apoe−/− mice.

To corroborate the transcriptome analysis data, we functionally examined adhesive and migratory capacity by an in vitro transendothelial migration (TEM) assay, using TNF-α stimulated Human Arterial Endothelial Cells (HAEC) and monocytes. We observed that when monocytes were pre-treated with TRAF6i-HDL, transendothelial migration of monocytes was markedly decreased (Fig. 5e, Supplementary Fig. 7, Supplementary movie 3). This confirms our finding from the whole transcriptome analysis. An additional beneficial effect of TRAF6i-HDL may be mediated through effects on endothelial cells. When TNF-α stimulated HAECs were treated, decreased transendothelial migration of untreated monocytes was observed. The strongest decrease in transendothelial migration was observed when both HAECs and monocytes were treated (Fig. 5e). Altogether, these data show that decreased monocyte infiltration in the plaque is an important mechanism by which TRAF6i-HDL exerts its effect on plaque inflammation, and may be mediated by TRAF6i-HDL's effect on monocyte migratory capacity as well as by effects on the endothelium.

To ultimately establish that the decreased numbers of monocytes and macrophages in the plaque resulted in decreased plaque inflammation, we performed fluorescence molecular tomography fused with computed tomography (FMT/CT) imaging to visualize protease activity in the aortic sinus area. Control (n=8) and TRAF6i-HDL (n=7) treated Apoe−/− mice all received one injection of an activatable pan-cathepsin protease sensor 24 hours before imaging. The protease sensor is taken up by activated macrophages, followed by cleavage of the protease sensor within the endolysosome, yielding fluorescence as a function of enzyme activity. TRAF6i-HDL therapy decreased protease activity by 60% (p=0.002, Fig. 5f).

### TRAF6i-HDL's toxicity and effects on the immune system in atherosclerotic mice and non-human primates.

In atherosclerotic mice, one week TRAF6i-HDL treatment had no effect on erythrocytes, platelets or leukocyte levels (Supplementary Table. 5). The number of reticulocytes was somewhat increased in both the rHDL and TRAF6i-HDL groups, compared to control. It was apparently not caused by SMI 6877002. ApoA-1 is not known to have an effect on erythropoiesis. The number of erythrocytes was unchanged and we did not observed signs of red cell destruction. The numbers of T cells and B cells in bone marrow, blood and spleen were not affected by TRAF6i-HDL therapy (Supplementary Fig. 5a & b). No toxic effects were observed on kidney and hepatic function, although alkaline phosphatase was somewhat increased (Supplementary Table. 6). Lipids, glucose, protein and electrolytes were unaffected.

Subsequently, we investigated TRAF6i-HDL's potential adverse immune effects on evoking or suppressing systemic inflammatory responses, by measuring serum cytokines and chemokines. Interleukin 6 (IL-6), interleukin 1β (IL-1β), chemokine (C-C motif) ligand 2 (CCL2), tissue necrosis factor α (TNFα), and serum amyloid P-component (SAP) levels were not affected (Fig. 6a).

Next, we investigated if CD40-TRAF6 inhibition affects the response of macrophages (RAW264.7 cells) to an LPS stimulus in vitro. We found that the LPS-induced NFκB activation is not inhibited by CD40-TRAF6 inhibition (Figure 6b). This observation was reproduced in bone marrow-derived macrophages (BMDMs) from C57BL/6 mice, which were stimulated with LPS and the agonistic CD40 antibody FGK45 (Fig 6c). RNA was isolated from BMDMs to asses CCL2 expression as a marker for macrophage activation. Incubation with TRAF6i-HDL did not affect CCL2 RNA expression. Altogether these data indicate our nanoimmunotherapy has a favorable immunologic safety profile. Of note, the bare CD40-TRAF6 inhibiting compound was previously investigated in a sepsis model, and no signs of an incompetent immune response were found. In fact, survival was improved[8].

In order to assess the translatability of TRAF6i-HDL therapy in non-human primates, we performed comprehensive blood testing and histological analysis. Six non-human primates were used for complete hematological analyses, post mortem histological analysis and blood chemistry analysis. The non-human primates were injected with either control or a single dose of TRAF6i-HDL (1 mg/kg) and sacrificed after 72 hours.

Complete blood count data from 7 time points within 72 hours after injection showed no differences between control and TRAF6i-HDL treated animals in white blood cells, monocytes, neutrophils, lymphocytes, red blood cells, platelets or any of the other indices. (Fig. 6e, Supplementary Fig. 8a).

Since the major accumulation site of the nanoparticles is in the liver, it is paramount to assess whether our therapy had toxic effects on this organ. Based on what is known from previous studies, we would not expect liver toxicity from CD40-TRAF6 inhibition. Under physiologic conditions, CD40 expression by hepatocytes is negligible. Therefore, CD40-TRAF6 inhibition is unlikely to affect hepatocytes.[19] Under pathological conditions,

hepatocytes express CD40, which renders stimulation of CD40 signaling harmful.[20,21] Our nanoimmunotherapy does the opposite and — under pathological conditions — may therefore exert a therapeutic benefit. Having said that, blood chemistry analysis confirmed that TRAF6i-HDL had no toxic effect on the liver (Fig. 6e). This was corroborated by liver histology (H&E) which showed no signs of tissue damage or disturbances in tissue architecture (Fig. 6f).

Additionally, blood chemistry analysis showed no signs of renal, pancreatic or muscle cell toxicity in the TRAF6i-HDL treated group as compared to the control group (Fig. 6e). Furthermore, lipid, glucose, and protein (albumin and globulin) levels were equal in both groups (Fig. 6e, Supplementary Fig. 8b). Electrolytes were also unaffected (Supplementary Fig. 8b). Kidneys and spleen histology (H&E) showed no signs of tissue damage or disturbances in tissue architecture (Fig. 6f).

## Discussion

We have described the development and evaluation of an HDL-based nanoimmunotherapy (TRAF6i-HDL) that modulates the CD40-TRAF6 interaction in monocytes and macrophages. Our data show that TRAF6i-HDL has a strong affinity for monocytes and macrophages in the hematopoietic organs, blood, and atherosclerotic lesions. A single week of therapy rapidly reduced plaque macrophage content, which can in part be attributed to the inhibition of monocyte recruitment, mediated through impairment of monocyte migratory capacity and potential additional effects on the endothelium. The fact that TRAF6i-HDL proved to be safe in non-human primates supports the translational potential of this therapy.

Taking a multiparametric approach, we not only teased out TRAF6i-HDL's therapeutic potential, but we also highlight the significance of integrating advanced in vivo imaging techniques to study its in vivo behaviour. Particularly, the PET/MRI data acquired in non-human primates provide compelling information about TRAF6i-HDL's distribution kinetics in a species closely related to humans.

The CD40-CD40L signaling axis has long been recognized to play an imperative role in eliciting immune responses in atherosclerosis[2-5]. While its identification gave rise to high anticipation, therapeutic targeting of this costimulatory receptor-ligand pair proved cumbersome. An anti-CD40L antibody was effective in diminishing atherosclerosis development in mice[3-5], but thromboembolic complications due to CD40 expressed on platelets prohibited its application in humans[22,23]. Furthermore, CD40 is expressed on B lymphocytes, and prolonged blocking would impair their maturation, causing immunodeficiency[24]. In the current study, we addressed these issues by targeting TRAF6's interaction with the cytoplasmic domain of CD40 in monocytes and macrophages. We did this by using HDL as a nanocarrier for a small molecule inhibitor of CD40-TRAF6 interaction. Our data show that our HDL based nanoimmunotherapy exposed over 80% of monocytes and macrophages to its cargo, while lymphocytes did not take up any nanoparticles. These observations corroborate our previous work on targeting efficiency of HDL based drug delivery[25].

We also aimed to minimize drug exposure by using short duration of therapy of only a single week. Previous therapeutic studies targeting the CD40-CD40L signaling axis used prolonged treatment times[3-5]. The fact that we found a 49% and 66% decrease in plaque Ly6C$^{hi}$ monocyte and macrophage content within one week signifies the high potency of TRAF6i-HDL nanoimmunotherapy. Of note, we proved the contribution of apoA-I to the therapeutic effect of TRAF6i-HDL to be minor. We used 4 infusions of 9 mg/kg apoA-I, which is relatively low compared to previously published studies[26], and we found no effects of empty HDL on plaque monocyte or macrophage content compared to controls.

The mechanism by which TRAF6i-HDL decreased plaque inflammation on such a short timescale can for an important part be explained by decreased monocyte recruitment. In general, plaque macrophage content is determined by a balance of monocyte recruitment as well as macrophage proliferation, apoptosis and migratory egress. The first two processes are considered the most important determinants[10,27-29]. Our data did not reveal an effect on macrophage proliferation, apoptosis or migratory egress. We did however observe a decrease in plaque Ly6C$^{hi}$ monocyte content while blood monocyte count was unaffected, indicative of decreased monocyte recruitment. This is in line with previous observations in a knockout mouse model with defective CD40-TRAF6 signaling. In a study by Lutgens et al. CD40-T6$^{-/-}$ mice were used to investigate the migratory capacity of monocytes and macrophages [7]. By performing in vivo intravital microscopy it was shown that Ly6C$^{hi}$ monocytes displayed impaired luminal adhesion to the wall of carotid arteries. Furthermore, CD40$^{-/-}$ as well as CD40-T6$^{-/-}$ macrophages displayed an impaired migration toward CCL2 in an *in vitro* Transwell migration assay[7]. In the current study, the comparative whole transcriptome analysis and *in vitro* monocyte migration assay confirmed that CD40-TRAF6 inhibition affects monocyte recruitment. We observed a differental expression of genes involved in “focal adhesion”. Rhoa, Rap1a and Rap1b, involved in activating integrins, were among the genes that were significantly downregulated. Although the differential gene expression was investigated in plaque monocytes and macrophages, we deem it likely that TRAF6i-HDL affects myeloid cells systemically. We observed nanoparticle uptake by myeloid cells in the hematopoietic organs, and TRAF6i-HDL treatment increased Ly6C$^{hi}$ monocytes the bone marrow, blood and spleen. Why Ly6C$^{hi}$ monocytes were increased in these tissues was not investigated, but may be related to either increased production or decreased mobilization of these cells.

In addition to treatment effects on monocyte and macrophages, TRAF6i-HDL may also have an effect on the endothelium. Monocyte infiltration into atherosclerotic lesions involves a close dialogue between monocytes and the endothelium. Activated endothelial cells express adhesion molecules that interact with glycosylated ligands and integrins expressed by monocytes. Although we did not investigate the uptake of TRAF6i-HDL by endothelial cells *in vivo*, we did observe in an *in vitro* assay that TRAF6i-HDL inhibits monocyte transmigration through the endothelium. This suggests that beneficial effects of TRAF6i-HDL on the endothelium may contribute to the observed decrease in monocyte recruitment.

Our data show high monocyte kinetics in atherosclerosis, which corroborates observations in previous studies[11,12,27-29]. In fact, decreased recruitment was shown to cause over 70% reduction in plaque macrophage content within 4 weeks[28]. Vice versa, a sudden increase in

monocyte recruitment, induced by myocardial infarction, caused a marked increase in plaque macrophage content within 1-3 weeks[29]. These observations are in line with our findings of decreased monocyte recruitment causing a 66% decrease of plaque macrophage content within one week.

Concerning the translatability of our therapy, we performed extensive experiments on pharmacokinetics, biodistribution and safety in non-human primates. The use of reconstituted HDL has previously proved to be safe in humans with apoA-I doses of 40 mg/kg[30,31].Since we used 1.8 mg/kg apoA-I, this poses no safety issues. Scaling up the production to a magnitude that would suffice for application in humans is feasible. Adequate amounts of apoA-1 can be obtained from human plasma (native apoA-I), bacteria or transgenic plants (recombinant apoA-I), or synthetically[32-35]. These methods have been applied in large clinical trials in humans[35-37]. Scaling the reconstitution of drug loaded HDL nanoparticles can be done with high pressure homogenization-based approaches or microfluidics[38].

The small molecule inhibitor of CD40-TRAF6 interaction that was recently developed has not been evaluated in humans yet. Biodistribution of $^{89}$Zr labeled TRAF6i-HDL was consistent with our previous observations with $^{89}$Zr labeled HDL in murine, rabbit, and porcine atherosclerosis models[39]. We observed the highest accumulation in the liver, spleen and kidneys. The liver and kidneys are the main sites of apoA-I and HDL catabolism, and the spleen is the major secondary lymphoid organ containing many myeloid cells that clear the nanoparticles from the circulation. There were no signs of toxic effects in the liver, kidney or spleen and all tissues showed normal tissue architecture on histological analysis. Furthermore, complete blood count did not show any effects on the numbers of platelets, lymphocytes, monocytes, neutrophils or red blood cells. Safety data were assessed up until 72 post administration. Long-term safety was not addressed in the current study.

Until recently, no therapies were evaluated that are specifically aimed at reducing vascular inflammation. Statins are known to have beneficial cardiovascular effects beyond cholesterol lowering[40]. Currently, chronic therapy with low dose methotrexate is being investigated in a large Phase III clinical trial[41]. A recently published Phase III clinical trial showed that chronic therapy with an IL-1β monoclonal antibody decreased the cardiovascular event rate[18]. This trial is the first to provide clinical evidence that immunotherapy can be beneficially applied in cardiovascular disease. The effect of chronic IL-1β antibody therapy was however modest, with a 2% absolute risk reduction in the primary endpoint and came at the cost of a higher incidence of fatal infection. We specifically designed our nanoimmunotherapy to rapidly suppress plaque inflammation in patients at high risk of cardiovascular events. While targeted delivery enhances efficacy, its short-term application minimizes the risks associated with prolonged immunosuppression. Patients admitted for an acute coronary syndrome may be an appropriate population for such induction therapy of inflammation since they have a markedly increased risk of recurrent myocardial infarction of up to 17.4% within the first year[42]. Recent studies have proposed that it is the initial myocardial infarction itself that evokes monocyte recruitment to atherosclerotic plaques causing them to become inflamed and vulnerable for plaque rupture[29]. In this

pathophysiological context, our concept of rapid suppression of monocyte recruitment in the vulnerable phase might be relevant.

In summary, this study describes a rapid induction therapy to treat inflammation in atherosclerosis, by modulating CD40-TRAF6 signaling in monocytes and macrophages. Our infusible HDL-based nanoimmunotherapy has potential for clinical translation, as attested by the favorable safety data in non-human primates.

## Methods

### Synthesis and characteristics of TRAF6i-HDL

The synthesis of TRAF6i-HDL was based on a previously published method[25,43]. In short, the CD40-TRAF6 inhibitor 6877002[8] was combined with 1-myristoyl-2-hydroxy-sn-glycero-phosphocholine (MHPC) and 1, 2-dimyristoyl-sn-glycero-3-phosphatidylcholine (DMPC) (Avanti Polar Lipids) in a chloroform/methanol mixture (9:1 by volume) and then dried in a vacuum, yielding a thin lipid film. A PBS solution of human apolipoprotein A1 (apoA-I) was added to the lipid film. The mixture was incubated at 37°C for 1 hour or until the film was hydrated and a homogenous solution was formed. The solution was then sonicated for 20 minutes to form TRAF6i-HDL nanoparticles. Subsequently, the solution was purified by multiple centrifugal filtration steps. For targeting, imaging and biodistribution experiments, analogs of TRAF6i-HDL were prepared through incorporation of the fluorescent dyes DiR or DiO (Invitrogen) in the core, or the phospholipid chelator DSPE-DFO (1 mol % at the expense of DMPC), which allows radiolabeling with $^{89}Zr$[44].

TRAF6i-HDL was characterized using a combination of dynamic light scattering (DLS), transmission electron microscopy (TEM) and size exclusion chromatography (SEC). In addition, the Zeta potential was determined. Size was evaluated as function of time at 4 ºC by DLS and SEC. Drug release was measured by a dialysis method at 4 ºC and 37 ºC in PBS, as well as in fetal bovine serum (FBS) at 37 ºC. Finally, $^{89}Zr$ labeling stability was established by SEC.

### Animals and diet for the mouse studies

Female Apoe−/− mice (B6.129P2-Apoetm1Unc, n=103) were used for this study. All animal care and procedures were based on an approved institutional protocol from Icahn School of Medicine at Mount Sinai. Eight-week-old Apoe−/− mice were purchased from The Jackson Laboratory. All mice were fed a high-cholesterol diet (HCD) (0.2% weight cholesterol; 15.2% kcal protein, 42.7% kcal carbohydrate, 42.0% kcal fat; Harlan TD. 88137) for 12 weeks.

The treatment protocol in each experiment was identical: twenty-week-old Apoe−/− mice were randomly assigned to either control (phosphate buffered saline (PBS) infused in the same volume as in the other groups), empty rHDL or TRAF6i-HDL (5 mg/kg) groups. Mice were treated with 4 intravenous injections over 7 days, while kept on a HCD during treatment. Animals were sacrificed 24 hours after the last injection.

## Flow cytometry

Apoe−/− mice were euthanized and perfused with PBS, after which the aorta from the aortic root to the iliac bifurcation was gently cleaned from fat and collected. Whole aortas were put in an enzymatic digestion solution containing liberase TH (4 U/mL) (Roche), deoxyribonuclease (DNase) I (40 U/ml) (Sigma-Aldrich) and hyaluronidase (60 U/mL) (Sigma-Aldrich), minced and placed in a 37 °C incubator for 60 minutes. Cells were run through a 70 μm strainer, and twice spun down and resuspended in serum containing media. Spleens were weighed and pushed through a 70 μm cell-strainer, spun down, resuspended in red cell lysis buffer for 4 minutes, and then inactivated using serum containing media, spun down and resuspended in 1000 μL serum containing media per 100 mg of spleen tissue. EDTA treated blood was spun down, resuspended in red cell lysis buffer for 4 minutes, and then inactivated using serum containing media, spun down and resuspended in 100 μl of serum containing media. Bone marrow was obtained from a single femur. The intact femurs were rinsed with 70% ethanol followed by three subsequent washes in ice-cold sterile PBS. The epiphyses were cut off and the bone marrow was flushed out with PBS. Cells were run through a 70 μm strainer, spun down and resuspended in red cell lysis buffer for 30 seconds, and then inactivated using serum containing media, spun down and resuspended in 1000 μL of serum containing media. The following antibodies were used: F4/80-PE-Cy7 (clone BM8, BioLegend); CD11b-PerCP/ Cy5.5 (clone M1/70, BioLegend); CD11c–APC (clone N418, BioLegend); CD45-brilliant violet 510 (clone 30-F11, BioLegend); Ly-6C–PE (clone AL-21, BD Biosciences); Ly6C- FITC (clone AL-21), BD Biosciences); CD90.2-eFluor 450 (clone 53-2.1, eBioscience); CD90.2-PE (clone 53-2.1, BD Biosciences); Ter119-eFluor 450 (clone TER-119, eBioscience); NK1.1-eFluor 450 (clone PK136, eBioscience); NK1.1-PE (clone PK136, BD Biosciences); CD49b-eFluor 450 (clone DX5, eBioscience); CD45R-eFluor450 (clone RA3-6B2, eBioscience); Ly-6G-Pacific Blue (clone 1A8, BioLegend); Ly-6G-PE (clone 1A8, BD Biosciences); CD3-PE (clone 17A2; Biolegend); CD19-PE (clone 1D3, BD Bioscience). The antibody dilutions ranged from 1:200 to 1:100. Contribution of newly made cells to different populations was determined by in vivo labeling with bromodeoxyuridine (BrdU). Incorporation was measured using APC-conjugated anti-BrdU antibodies according to the manufacturer's protocol (BD APC-BrdU Kit, 552598). Monocytes and macrophages were identified using a method similar to one described previously[10-12]. Specifically, Ly6Chi monocytes were identified as CD11bhi, CD11clow, Lin-/low (with Lin defined as CD90.2+, CD45R+, CD49b+, NK1.1+, Ly-6G+, Ter119+ or CD90.2+, NK1.1+, Ly-6G+, CD19+, CD3+) F4/80low that were also Ly-6Chi. Macrophages were identified as CD11bhi, CD11clow, Lin-/low, F4/80hi, CD11-/low. Data were acquired on an LSRII flow cytometer (BD Biosciences) and analyzed with FlowJo v10.0.7 (Tree Star, Inc.).

## Histology and immunohistochemistry

Tissues for histological analysis were collected and fixed overnight in formalin and embedded in paraffin. Aortic roots were sectioned into 4 μm slices, generating a total of 90 - 100 cross-sections per root. Eight cross-sections were stained with hematoxylin and eosin (HE) and used for atherosclerotic plaque size measurement. Other sections were deparaffinized, blocked, incubated in 95°C antigen-retrieval solution (DAKO), and immunolabeled with either MAC-3 rat monoclonal antibody (1:30; BD Biosciences) or anti-

Ki67 rabbit polyclonal antibody (1:200, Abcam). Sirius red staining was used for analysis of collagen content. Antibody staining was visualized by either Immpact AMEC red (Vectorlabs) or diaminobenzidine (DAB). Sections were analyzed using a Leica DM6000 microscope (Leica Microsystems) or the VENTANA iScan HT slide scanner (Ventana).

## Laser capture microdissection and RNA sequencing

Laser capture microdissection (LCM) was performed on 24 aortic root sections (6 μm) as previously described (20). In short, frozen sections were dehydrated in graded ethanol solutions (70% twice, 95% twice, 100% once), washed with diethyl pyrocarbonate (DEPC) treated water, stained with Mayer's hematoxylin, eosin and cleared in xylene. For every 8 sections, 1 section was used for CD68 staining (Abdserotec, 1:250 dilution) which was used to guide the LCM. CD68 rich areas within the plaques were identified and cut out using the ArcturusXT LCM System. The collected CD68 positive cells were used for RNA isolation (PicoPure RNA Isolation Kit, Arcturus) and subsequent RNA amplification and cDNA preparation according to the manufacturers protocols (Ovation Pico WTA System, NuGEN). Quality and concentration of the collected samples were measured with the Agilent 2100 Bioanalyzer. RNA sequencing. Pair-end libraries were prepared and validated. The purity, fragment size, yield and concentration were determined. During cluster generation, the library molecules were hybridized onto an Illumina flow cell. Subsequently, the hybridized molecules were amplified using bridge amplification, resulting in a heterogeneous population of clusters. The data set was obtained using an lllumina HiSeq 2500 sequencer.

## Differential Expression and Function Annotation Analysis

The pair-ended sequencing reads were aligned to human genome hg19 using tophat aligner (bowtie2)[45]. Following read alignment, HTSeq[46] was used to quantify gene expression at the gene level based on GENCODE gene model release 22[47]. Gene expression raw read counts were normalized as counts per million using trimmed mean of M-values normalization method to adjust for sequencing library size difference among samples. Differential expressed genes between drug treatments and controls were identified using the Bioconductor package limma[48]. In order to correct the multiple testing problem, limma was used to calculate statistics and p-values in random samples after a permutation of labels. This procedure was repeated 1,000 times to obtain null t- statistic and p-value distribution for estimating the false discovery rate (FDR) of all genes. The differentially expressed (DE) genes were identified by a cutoff of corrected p-value less than 0.2. GO-function[49] was used to annotate the DE genes, and to find cellular components that significantly enriched with the DE genes. DE genes were also mapped to the Kyoto Encyclopedia of Genes and Genomes (KEGG) pathway with KEGG Mapper[50].

## Fluorescence molecular tomography with CT

Female Apoe−/− mice fed a high-cholesterol diet for 12 weeks, were treated with either four TRAF6i- HDL infusions (5 mg/kg, n=7) or saline (n=8) over 7 days. Five nanomoles of pan-cathepsin protease sensor (ProSense 680, PerkinElmer, Cat no. NEV10003) was intravenously administered 24 hours prior to imaging. For the FMT/CT imaging, animals were placed in a custom-built imaging cartridge, which was equipped for isoflurane administration during imaging. Animals were first scanned with high-resolution computed

tomography (CT; Inveon PET-CT, Siemens), with a continuous infusion of CT-contrast agent (isovue-370, Bracco Diagnostics) at a rate of 55 μL/min through a tail vein catheter. Animals were subsequently scanned with an FMT scanner (PerkinElmer) in the same cartridge. The CT X-ray source with an exposure time of 370–400 ms was operated at 80 kVp and 500 mA. Contrast-enhanced high-resolution CT images were used to localize the aortic root, which was used to guide the placement of the volume of interest for the quantitative FMT protease activity map. Image fusion relied on fiducial markers. Image fusion and analysis was performed with OsiriX v.6.5.2 (The Osirix Foundation, Geneva).

### Lipopolysaccharide (LPS) stimulation test in RAW 264.7 cells.

RAW264.7 cells, stably transfected with the 3x-κBluc plasmid[9], were incubated with the small molecules (10 μM) or vehicle for 1 h. Subsequently, cells were activated using (LPS) from E. coli (Sigma-Aldrich). After 2 h, cells were lysed, and substrate was added according to the manufacturer's protocol (Luc-screen system; Applied Biosystems). Emission was measured at 450 nm using the Wallac Victor II luminometer.

### In vitro LPS and FGK45 stimulation test in bone marrow derived macrophages.

Bone marrow (BM) cells were isolated from C57BL/6 mice, and cultured in RPMI supplemented with 15% L929-conditioned medium to generate BM-derived macrophages (BMDMs). One hour before activation, BMDMs were incubated with TRAF6i-HDL (10 μM). BMDMs were activated by the agonistic CD40 antibody FGK45 (30 μg/ml, Bioceros BV) and LPS (1 ng/ml, Sigma) for 6 hours. RNA was isolated from BMDMs and reverse transcribed using an iScript cDNA synthesis kit (Bio-Rad). Quantitative (q)PCR was performed with a SYBR Green PCR kit (Applied Biosystems) on a ViiA 7 real-time PCR system (Applied Biosystems). Primer sequences are available upon request.

### Radiolabeling of HDL nanoparticles

Ready-to-label HDL nanoparticles were prepared by including 1 mol % the phospholipid-chelator DSPE-DFO in the formulation mix at the expense of DMPC. The DFO- containing nanoparticles were then labeled with Zirconium-89 ($^{89}$Zr) as previously described[39]. Briefly, the nanoparticles were reacted with $^{89}$Zr-oxalate in phosphate buffered saline (PBS, pH 7.1) at 37 °C for 1 hour. Purification was carried out by centrifugal filtration using 10 kDa molecular weight cut-off filter tubes, and washing twice with fresh sterile PBS. The radiochemical yield was 90 ± 4% (n=3) and radiochemical purity > 97%, as determined by size exclusion chromatography.

### Pharmacokinetics, biodistribution and PET/CT imaging studies in mice

Female Apoe−/− mice fed a high-cholesterol diet for 12 weeks (n=4, 25.5 ± 2.6 g body weight) were injected with $^{89}$Zr-TRAF6i-HDL nanoparticles (183 ± 16 μCi, 5 mg TRAF6i-HDL/kg). At predetermined time points (2, 15 and 30 min, and 1, 4, 8 and 24 hours) blood samples were taken, weighed and measured for radioactivity content using a 2470 Wizard automatic gamma counter (Perkin Elmer). Data were converted to percentage of injected dose per gram tissue [%ID/g], plotted in a time-activity curve and fitted using a non-linear

two-phase decay regression in Prism GraphPad (GraphPad Software inc, USA). A weighted blood radioactivity half-life (t1/2) was finally calculated.

Twenty-four hours after injection, the animals were scanned on an Inveon PET/CT scanner (Siemens Healthcare Global) under isoflurane/oxygen gas mixture anesthesia (2% for induction, 1 % for maintenance). The PET static scan recorded a minimum of 25 million coincident events and lasted 10 min. The energy and coincidence timing windows were 350–700 keV and 6 ns, respectively. Image data were normalized to correct for nonuniformity of response of the PET, dead-time count losses, positron branching ratio, and physical decay to the time of injection, but no attenuation, scatter, or partial-volume averaging correction was applied. The counting rates in the reconstructed images were converted to activity concentrations (%ID/g) by use of a system calibration factor derived from the imaging of a mouse-sized water-equivalent phantom containing $^{89}$Zr. Images were analyzed using ASIPro VMTM (Concorde Microsystems) and Inveon Research software (Siemens Healthcare Global). Quantification of activity concentration was done by averaging the maximum values in at least 5 regions of interest drawn on adjacent slices of the tissue of interest. Whole body standard low magnification CT scans were performed with the X-ray tube setup at a voltage of 80 kV and current of 500 μA. The CT scan was acquired using 120 rotational steps for a total of 220 degrees yielding and estimated scan time of 120 seconds with an exposure of 145 ms per frame. Immediately after the PET/CT scan, animals were sacrificed and perfused with PBS. Tissues of interest (liver, kidneys, spleen, lungs, muscle, heart, aorta, bone and brain) were collected, blotted and weighed. Radioactivity was measured by gamma counting and radioactivity concentration expressed as percentage of injected dose per gram [%ID/g].

### Autoradiography

Following radioactivity counting, aortas were placed in a film cassette against a phosphorimaging plate (BASMS-2325, Fujifilm, Valhalla, NY) for 24 hours at −20 °C in order to determine radioactivity distribution. The plates were read at a pixel resolution of 25μm with a Typhoon 7000IP plate reader (GE Healthcare, Pittsburgh, PA).

### Ex vivo near infrared fluorescence imaging (NIRF)

Female Apoe−/− mice fed a high-cholesterol diet for 12 weeks, received a single intravenous injection with DiR (0.5 mg/kg) labeled TRAF6i-HDL (5 mg/kg, n=2) or saline (n=1). Mice were sacrificed 24 hours after the injection and perfused with 60 mL PBS. Liver, spleen, lung, kidneys, heart and muscle tissue were collected for NIRF imaging. Fluorescent images were acquired with the IVIS 200 system (Xenogen), with a 2 second exposure time, using a 745 nm excitation filter and an 820 nm emission filter. ROIs were drawn on each tissue with software provided by the vendor, after which a quantitative analysis was done with the average radiant efficiency within these ROIs.

### Blood tests in mice

In mice, blood was collected by heart puncture at the time of sacrifice. Serum was sent to IDEXX laboratories (Totowa, New Jersey, USA) and analyzed with an Olympus AU400

chemistry analyzer. Whole blood was collected in EDTA containing tubes and analyzed with an IDEXX procyte DX hematology analyzer for complete blood count analysis.

For the multiplex analysis, mice were intravenously injected with TRAF6i-HDL at 5 mg/kg or with PBS. Serum was collected 24 hours after injection. Levels of IL-6, TNFα, CCL2, IL-1β and SAP were measured using Milliplex detection kits MAP2MAG-76K and MCYTOMAG-70k (Millipore Corporation, St Charles, MO, USA). Samples were run in triplicate.

### In vitro transendothelial monocyte migration assay

Human Arterial Endothelial Cells (HAEC, purchased from Lonza (Baltimore, MD)) were cultured to confluency and subsequently stimulated with TNF-α (10 ng/ml) overnight. HAECs were either pre-incubated for 30 minutes with 35 μM of CD40-TRAF6 inhibitor or DMSO as solvent control. Subsequently, the culture medium containing the compound was replaced by regular EMG-2 medium and 20 minutes later, the TEM assay was performed. The assay was either performed with monocytes pre-treated for 30 minutes with 35 μM of CD40-TRAF6 inhibitor or DMSO as solvent control. Pre-treatment was performed under shaking conditions in polypropylene, low-retention tubes (Falcon, Corning Inc, NY) to minimize adhesion during the incubation step. Monocytes were added at a concentration of 37 °C, 5% $CO_2$ and then fixed with 3.7% formaldehyde 30 minutes after addition (Sigma-Aldrich, Zwijndrecht, the Netherlands). Multiple images were recorded per well with a Leica DMi8 microscope (Plan-Apochromat 10x/0.25 Phaco 1 objective; Leica, Wetzlar, Germany). Adhered (bright morphology) and transmigrated monocytes (dark morphology) were quantified using the cell counter plugin (http://rsbweb.nih.gov/ij/plugins/cell-counter.html)) in the Image-J software (http://rsb.info.nih.gov/nih-image/)). version 2.00-rc-43.

### Non-human primate studies

Adult male cynomolgus monkeys (Macaca fascicularis) were used for the non-human primate studies conducted at the University of Kentucky and Icahn School of Medicine at Mount Sinai. The average weight of the animals was 7.3 ± 1.98 kg (mean ± SD). Monkeys were pair-housed when possible in climate-controlled conditions with 12-hour light/dark cycles. Monkeys were provided water ad libitum and fed Teklad Global 20% Protein Primate Diet. For the experiment at the University of Kentucky, the six male monkeys were used. After an overnight fast, monkeys were anesthetized with ketamine (5 mg/kg) and dexmedetomidine (0.0075-0.015 mg/kg), and blood was collected from the femoral vein. The monkeys were then injected intravenously via the saphaneous vein with either vehicle (PBS, USP grade) or TRAF6i-HDL such that the dose of CD40-TRAF6 inhibitor 6877002 was 1 mg/kg. Blood was collected 15 minutes, 6, 12, 24, and 48 hours post-injection. Following the blood draw anesthesia was reversed with atipamezole (0.075-0.15 mg/kg). 72 hours post-injection, fasted monkeys were anesthetized with ketamine (25 mg/kg), bled a final time, and euthanized by exsanguination with whole-body saline perfusion while anesthetized with isoflurane (3–5% induction, 1–2% maintenance). Tissues were promptly removed and fixed in 10% neutral-buffered formalin. Blood was subjected to complete blood count (CBC) test (ANTECH Diagnostics).

For the experiment at Icahn School of Medicine at Mount Sinai six female monkeys were used. For the $^{89}$Zr-PET/MRI imaging, animals were infused with 58.9 ± 17.9 MBq of $^{89}$Zr-labeled TRAF6i-HDL (1 mg/kg) and imaged by PET/MRI at different time points. Dynamic PET imaging was performed during the first 60 minutes after infusion. Additional PET/MRI scans were performed at 24, 48 and 72 hours. PET and MR images were acquired on a combined 3T PET/MRI system (Biograph mMR, Siemens Healthineers, Erlangen, Germany). On day 1, dynamic PET imaging was performed for 60 minutes using one bed position covering the chest and abdomen, directly after injection with $^{89}$Zr-labeled TRAF6i-HDL. Simultaneously, anatomical vessel wall MR images were acquired using a proton density (PD) weighted Sampling Perfection with Application optimized Contrasts using different flip angle Evolution (SPACE) sequence. MR imaging parameters were: acquisition plane, coronal; repetition time (TR), 1000 ms; echo time (TE), 79 ms; field of view (FOV), 300 × 187 mm2; number of slices, 144; number of averages, 4; bandwidth, 601 Hz/pixel; turbo factor (TF), 51; echo trains per slice, 4; echo train length, 192 ms; echo spacing, 3.7 ms; acquisition duration, 33 minutes and 36 seconds. After dynamic PET acquisition, static whole-body PET imaging was acquired from the cranium to the pelvis, using 3 consecutive bed positions, of 10 minutes each. Simultaneously with each bed, MR images were acquired as described above, except using only 1.4 signal average (acquisition duration, 11 min 44 seconds per bed). Whole-body PET and MR imaging was also performed at 24, 48 and 72 hours after injection, using 3 bed positions (PET duration per bed, 30 min; MR duration per bed, 33 minutes and 36 seconds). Whole-body MR images from each bed were automatically collated together by the scanner.

After acquisition, PET raw data from each bed were reconstructed and collated together offline using the Siemens proprietary e7tools with an Ordered Subset Expectation Maximization (OSEM) algorithm with Point Spread Function (PSF) correction. A dual-compartment (soft tissue and air) attenuation map was used for attenuation correction.

### Blood tests in non-human primates

In non-human primates blood was collected at 0 and 15 minutes and 6, 12, 24, 28, 48 and 72 hours after infusion. Serum was analyzed with an Olymus AU400 chemistry analyzer. Whole blood samples were also analyzed with an IDEXX procyte DX hematology analyzer. Levels of IL-6, TNFα and CCL2 were measured using Milliplex detection kits HCMP2MAG-19k and PRCYTOMAG-40k (Millipore Corporation, St Charles, MO, USA). Samples were run in duplicate.

### Statistical analysis

Continuous variables are expressed as means ± standard deviation, unless otherwise stated. Significance of differences were calculated by use of the nonparametric Mann-Whitney U tests and Kruskal-Wallis tests. Probability values of $P<0.05$ were considered significant. Statistical analyses were done using IBM Statistical Package for the Social Sciences (SPSS) version 25.

### Study approval

All animal care, procedures and experiments were based on approved institutional protocols from Icahn School of Medicine at Mount Sinai and the University of Kentucky Institutional Animal Care and Use Committee.

## Supplementary Material

Refer to Web version on PubMed Central for supplementary material.

## Acknowledgments

The authors would like to thank the Icahn School of Medicine at Mount Sinai's core facilities: flow cytometry core, quantitative PCR core, TMII's preclinical imaging core. This study was funded by National Institutes of Health grants R01 HL118440, R01 HL125703 and P01 HL131478 (all to W.J.M.M.) and R01 EB009638 (Z.A.F.), as well as the NWO grant ZonMW Veni 016156059 (R.D.), and ZonMW Vidi 91713324 (W.J.M.M.), and European Research Council (ERC Con to E.L.) and the DFG (SFB 1123-A5 to E.L).

## References

1. Swirski FK, Nahrendorf M Leukocyte behavior in atherosclerosis, myocardial infarction, and heart failure. Science. 339, 161–6 (2013). [PubMed: 23307733]
2. Schönbeck U, Libby P CD40 signaling and plaque instability. Circ. Res. 89, 1092–103 (2001). [PubMed: 11739273]
3. Lutgens E et al. Requirement for CD154 in the progression of atherosclerosis. Nat. Med. 5, 1313–6 (1999). [PubMed: 10546000]
4. Mach F, Schönbeck U, Sukhova GK, Atkinson E, Libby P Reduction of atherosclerosis in mice by inhibition of CD40 signalling. Nature. 394, 200–3 (1998). [PubMed: 9671306]
5. Schönbeck U, Sukhova GK, Shimizu K, Mach F, Libby P Inhibition of CD40 signaling limits evolution of established atherosclerosis in mice. Proc. Natl. Acad. Sci. U S A. 97, 7458–63 (2000). [PubMed: 10861012]
6. Lutgens E et al. Both early and delayed anti-CD40L antibody treatment induces a stable plaque phenotype. Proc. Natl. Acad. Sci. U S A. 97, 7464–9 (2000). [PubMed: 10861013]
7. Lutgens E et al. Deficient CD40-TRAF6 signaling in leukocyte prevents atherosclerosis by skewing the immune response toward an antiinflammatory profile. J. Exp. Med. 207, 391–404 (2010). [PubMed: 20100871]
8. Zarzycka B et al. Discovery of small molecule CD40-TRAF6 inhibitors. J. Chem. Inf. Model. 55, 294–307 (2015). [PubMed: 25622654]
9. Chatzigeorgiou A et al. Blocking CD40-TRAF6 signaling is a therapeutic target in obesity-associated insulin resistance. Proc. Natl. Acad. Sci. U S A. 111, 2686–91 (2014). [PubMed: 24492375]
10. Robbins CS et al. Local proliferation dominates lesional macrophage accumulation in atherosclerosis. Nat. Med. 19, 1166–72 (2013). [PubMed: 23933982]
11. Swirski FK et al. Ly-6Chi monocytes dominate hypercholesterolemia-associated monocytosis and give rise to macrophages in atheromata. J. Clin. Invest. 117, 195–205 (2007). [PubMed: 17200719]
12. Swirski FK et al. Monocyte accumulation in mouse atherogenesis is progressive and proportional to extent of disease. Proc. Natl. Acad. Sci. U S A. 103, 10340–5 (2006). [PubMed: 16801531]
13. Kiener PA et al. Stimulation of CD40 with purified soluble gp39 induces proinflammatory responses in human monocytes. J Immunol. 155, 4917–25 (1995). [PubMed: 7594496]
14. Iloki Assanga SB et al. Cell growth curves for different cell lines and their relationship with biological activities. Int. J. Biotechnol. Mol. Biol. Res. 4, 60–70 (2013).
15. Imhof BA Aurrand-Lions M Adhesion mechanisms regulating the migration of monocytes. Nat. Rev. Immunol. 4, 432–44 (2004). [PubMed: 15173832]

16. Wenger GD, O'Dorisio MS Induction of cAMP-dependent protein kinase I during human monocyte differentiation. J. Immunol. 134, 1836–43 (1985). [PubMed: 2981923]
17. Chinetti-Gbaguidi G, Colin S, Staels B Macrophage subsets in atherosclerosis. Nat. Rev. Cardiol. 12, 10–7 (2015). [PubMed: 25367649]
18. Ridker PM et al. Antiinflammatory therapy with Canakinumab for atherosclerotic disease. N. Engl. J. Med. doi: 10.1056/NEJMoa1707914 (2017).
19. Afford SC et al. CD40 activation induces apoptosis in cultured human hepatocytes via induction of cell surface fas ligand expression and amplifies fas-mediated hepatocyte death during allograft rejection. J Exp Med. 189, 441–6 (1999). [PubMed: 9892626]
20. Bhogal RH et al. Activation of CD40 with platelet derived CD154 promotes reactive oxygen species dependent death of human hepatocytes during hypoxia and reoxygenation. PLoS One. 7, e30867 (2012). [PubMed: 22295117]
21. Tang Y et al. Up-regulation of the expression of costimulatory molecule CD40 in hepatocytes by hepatitis B virus X antigen. Biochem Biophys Res Commun. 384, 12–7 (2009). [PubMed: 19336218]
22. Kawai T, Andrews D, Colvin RB, Sachs DH, Cosimi AB Thromboembolic complications after treatment with monoclonal anti-body against CD40 ligand. Nat. Med. 6, 114 (2000).
23. André P et al. CD40L stabilizes arterial thrombibyabeta3 integrin—dependent mechanism. Nat. Med. 8, 247–52 (2002). [PubMed: 11875495]
24. Ahonen C et al. The CD40-TRAF6 axis controls affinity maturation and the generation of long-lived plasma cells. Nat. Immunol. 3, 451–6 (2002). [PubMed: 11967542]
25. Duivenvoorden R et al. A statin-loaded reconstituted high-density lipoprotein nanoparticle inhibits atherosclerotic plaque inflammation. Nat. Commun. 5, 3065 (2014). [PubMed: 24445279]
26. Shah PK et al. Effects of recombinant apolipoprotein A-I(Milano) on aortic atherosclerosis in apolipoprotein E-deficient mice. Circulation. 97, 780–5 (1998). [PubMed: 9498542]
27. Moore KJ, Sheedy FJ, Fisher EA Macrophages in atherosclerosis: a dynamic balance. Nat. Rev. Immunol. 13, 709–21 (2013). [PubMed: 23995626]
28. Potteaux S et al. Suppressed monocyte recruitment drives macrophage removal from atherosclerotic plaques of Apoe−/− mice during disease regression. J. Clin. Invest. 121, 2025–36 (2011). [PubMed: 21505265]
29. Dutta P et al. Myocardial infarction accelerates atherosclerosis. Nature. 487, 325–329 (2012). [PubMed: 22763456]
30. Nissen SE. et al. Effect of recombinant ApoA-I Milano on coronary atherosclerosis in patients with acute coronary syndromes: a randomized controlled trial. JAMA. 290, 2292–2300 (2003). [PubMed: 14600188]
31. Tardif JC. et al. Effects of reconstituted high-density lipoprotein infusions on coronary atherosclerosis: a randomized controlled trial. JAMA. 297, 1675–1682 (2007). [PubMed: 17387133]
32. Lerch PG et al. Production and characterization of a reconstituted high density lipoprotein for therapeutic applications. Vox Sang. 71, 155–64 (1996). [PubMed: 8912458]
33. Nykiforuk CL, et al. Expression and recovery of biologically active recombinant Apolipoprotein AI(Milano) from transgenic safflower (Carthamus tinctorius) seeds. Plant Biotechnol J. 9, 250–63 (2011). [PubMed: 20618764]
34. Sanchez-Gaytan BL et al. HDL-mimetic PLGA nanoparticle to target atherosclerosis plaque macrophages. Bioconjug Chem. 26, 443–51 (2015). [PubMed: 25650634]
35. Degoma EM, Rader DJ Novel HDL-directed pharmacotherapeutic strategies. Nat Rev Cardiol. 8, 266–77 (2011). [PubMed: 21243009]
36. Tardif JC et al. Effect of rHDL on Atherosclerosis-Safety and Efficacy (ERASE) Investigators. Effects of reconstituted high-density lipoprotein infusions on coronary atherosclerosis: a randomized controlled trial. JAMA. 297, 1675–82 (2007). [PubMed: 17387133]
37. Tardif JC et al. Effects of the high-density lipoprotein mimetic agent CER-001 on coronary atherosclerosis in patients with acute coronary syndromes: a randomized trial. Eur Heart J. 35, 3277–86 (2014). [PubMed: 24780501]

38. Kim Y et al. Single step reconstitution of multifunctional high-density lipoprotein-derived nanomaterials using microfluidics. ACS Nano. 7, 9975–83 (2013). [PubMed: 24079940]
39. Pérez-Medina C et al. In Vivo PET Imaging of HDL in Multiple Atherosclerosis Models. JACC Cardiovasc. Imaging. 9, 950–61 (2016). [PubMed: 27236528]
40. Ridker PM et al. Rosuvastatin to prevent vascular events in men and women with elevated C-reactive protein. N Engl J Med. 359, 2195–207 (2008). [PubMed: 18997196]
41. Everett BM et al. Rationale and design of the Cardiovascular Inflammation Reduction Trial: a test of the inflammatory hypothesis of atherothrombosis. Am. Heart. J. 166, 199–207 (2013). [PubMed: 23895801]
42. Stone GW et al. A prospective natural-history study of coronary atherosclerosis. N. Engl. J. Med. 364, 226–35 (2011). [PubMed: 21247313]
43. Jonas A Reconstitution of high-density lipoproteins. Methods Enzymol. 128, 553–82 (1986). [PubMed: 3724523]
44. Pérez-Medina C et al. PET Imaging of Tumor-Associated Macrophages with 89Zr-Labeled High-Density Lipoprotein Nanoparticles. J. Nucl. Med. 56, 1272–7 (2015). [PubMed: 26112022]
45. Langmead B, Salzberg SL Fast gapped-read alignment with Bowtie 2. Nat. Methods. 9, 357–9 (2012). [PubMed: 22388286]
46. Anders S, Pyl PT, Huber W HTSeq - a Python framework to work with high-throughput sequencing data. Bioinformatics. 31, 166–9 (2015). [PubMed: 25260700]
47. Mudge JM, Harrow J Creating reference gene annotation for the mouse C57BL6/J genome assembly. Mamm. Genome. 26, 366–78 (2015). [PubMed: 26187010]
48. Ritchie ME et al. Limma powers differential expression analyses for RNA-sequencing and microarray studies. Nucleic Acids Res. 43, e47 (2015). [PubMed: 25605792]
49. Wang J et al. GO-function: deriving biologically relevant functions from statistically significant functions. Brief Bioinform. 13, 216–27 (2012). [PubMed: 21705405]
50. Kanehisa M, Goto S, Sato Y, Furumichi M, Tanabe M KEGG for integration and interpretation of large-scale molecular data sets. Nucleic Acids Res. 40, D109–14 (2012). [PubMed: 22080510]

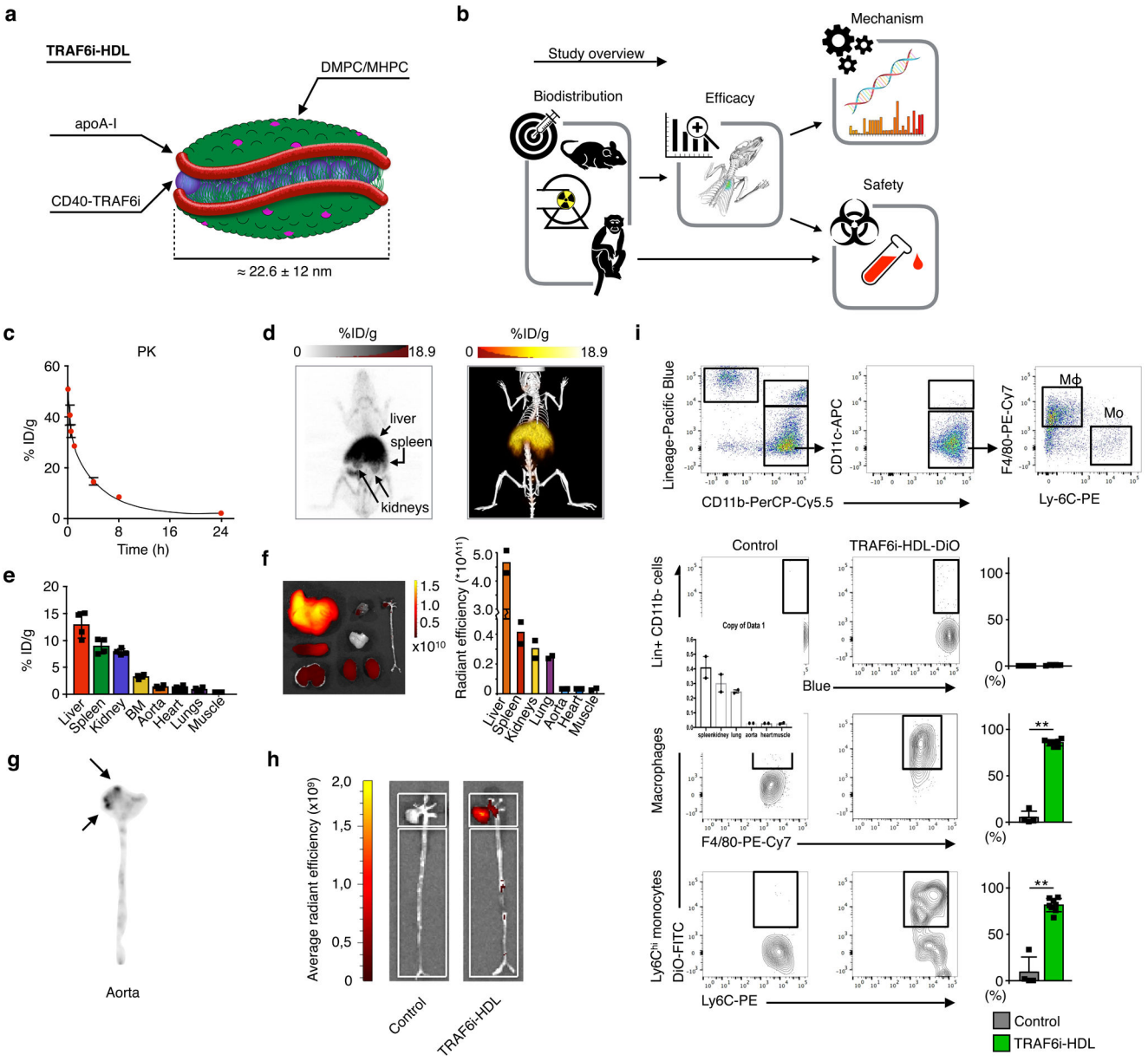


**Figure 1. TRAF6i-HDL biodistribution and uptake.**

(**a**) A schematic representation of TRAF6i-HDL, which was constructed by combining human apoA-I, lipids (DMPC and MHPC) and a small molecule inhibitor of the CD40-TRAF6 interaction. (**b**) Study overview showing the subsequent steps that were taken to investigate TRAF6i-HDL's in vivo behavior and therapeutic efficacy. Eight-week old Apoe −/− mice were fed a high-cholesterol diet for 12 weeks and then received an intravenous injection with either $^{89}$Zr-, DiR or DiO core labeled TRAF6i-HDL nanoparticles. Twenty-four hours later, mice were used for PET/CT imaging or sacrificed for ex vivo NIRF imaging or flow cytometry analysis. (**c**) Pharmacokinetics of $^{89}$Zr-labeled TRAF6i-HDL in Apoe−\− mice (n=3), showing the blood decay curve. (**d**) Whole body three-dimensional rendered PET/CT fusion image at 24 hours post administration showing the highest uptake

in the liver, spleen and kidneys. (**e**) Gamma counting of the distribution of $^{89}$Zr-labeled TRAF6i-HDL at 24 hours post administration (n=4). Bars represent the mean and standard error of the mean. (**f**) Biodistribution 24 hours after infusion of DIO core labelled TRAF6i-HDL in Apoe−/− mice (n=2). Ex vivo near infrared fluorescence (NIRF) imaging, showing that the nanoparticles accumulates mostly in the liver, spleen and kidneys. (**g**) Autoradiography of the aorta shows visible TRAF6i-HDL accumulation in the aortic root (n=3), which is the preferential location of atherosclerosis development in the mouse model. (**h**) NIRF imaging of DiR core labeled TRAF6i-HDL distribution in mouse aorta (n=2), showing accumulation of TRAF6i-HDL in the aortic root area. (**i**) Flow cytometry data of whole mouse aortas (n=8) with DiO-labeled TRAF6i-HDL, showing high targeting efficiency of macrophages ($p=6.4E^{-3}$) and Ly6Chi monocytes ($p=6.5E^{-3}$), while lineage positive CD11b negative cells did not take up nanoparticles. ** $p < 0.01$. P-values were calculated with Mann-Whitney U tests (two sided). Bars represent the mean and standard error of the mean.

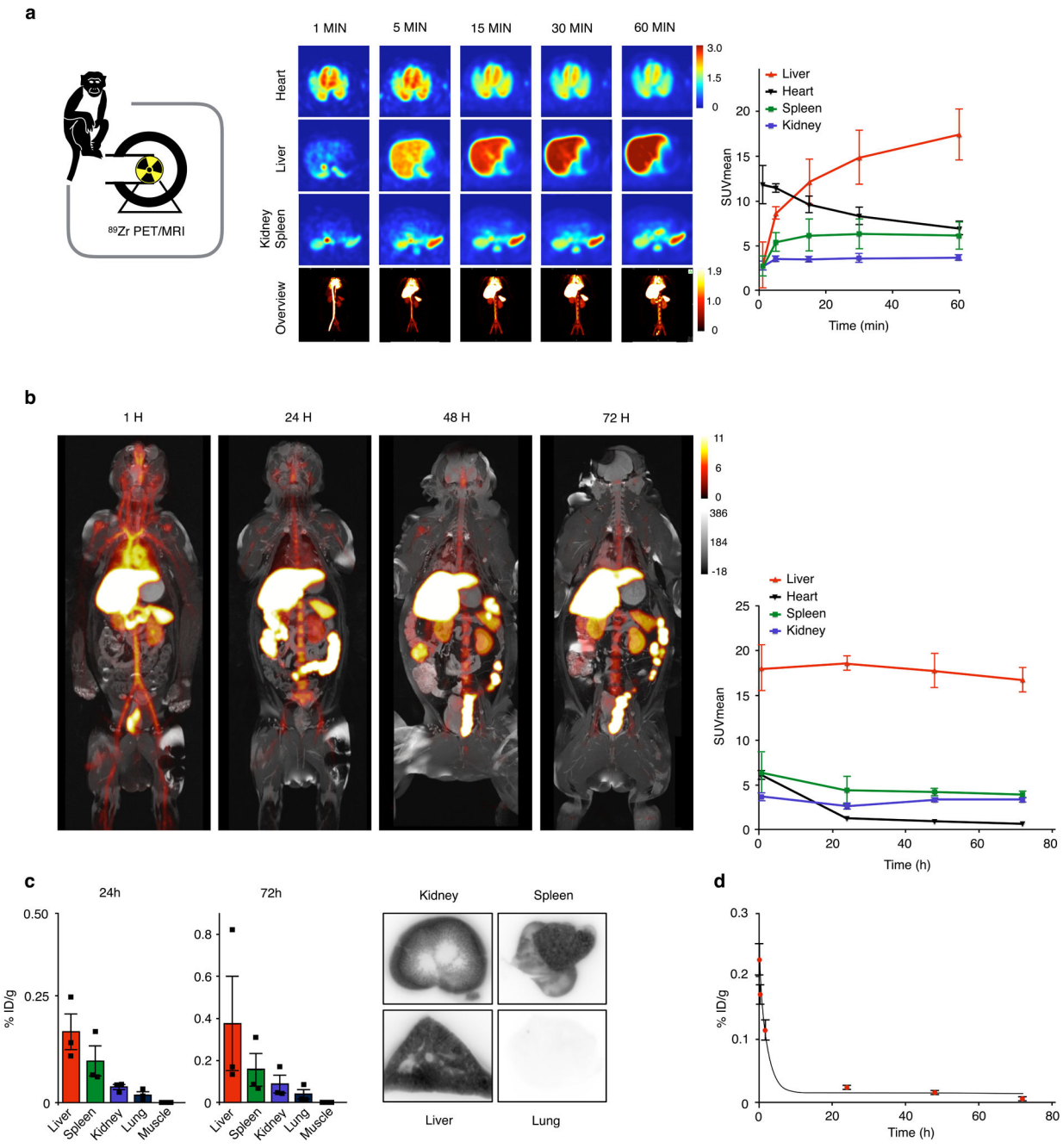


**Figure 2. TRAF6i-HDL biodistribution in non-human primates.**

Six non-human primates were infused with $^{89}$Zr-labeled TRAF6i-HDL (1 mg/kg). Dynamic PET images were acquired within 60 minutes after infusion. Static PET/MRI scans were performed at 24, 48 and 72 hours (See Supplementary movie 1 for three-dimensional rendered MRI data). NHP were sacrificed after 72 hours. Organs were collected for ex vivo analysis. (**a**) Dynamic PET images at 1, 5, 15, 30 and 60 minutes (n=3). Images are split up to visualize liver and other organs separately. The graph shows the quantified uptake in the represented organs at the different time points (See Supplementary movie 2 for a 3D representation of the distribution at 60 min). (**b**) Static PET/MR images at 24, 48 and 72

hours show the distribution and accumulation of TRAF6i-HDL. The graph shows the quantified uptake in the represented organs at the different time points (n=3 per timepoint). (**c**) Gamma counting distribution in NHPs at 24 and 72 hours post administration of $^{89}$Zr-TRAF6i-HDL (n=3). Bars represent the mean. (**d**) Blood time-activity curve for $^{89}$Zr-TRAF6i-HDL in non-human primates (n=3 per timepoint). Bars represent the standard error of the mean.

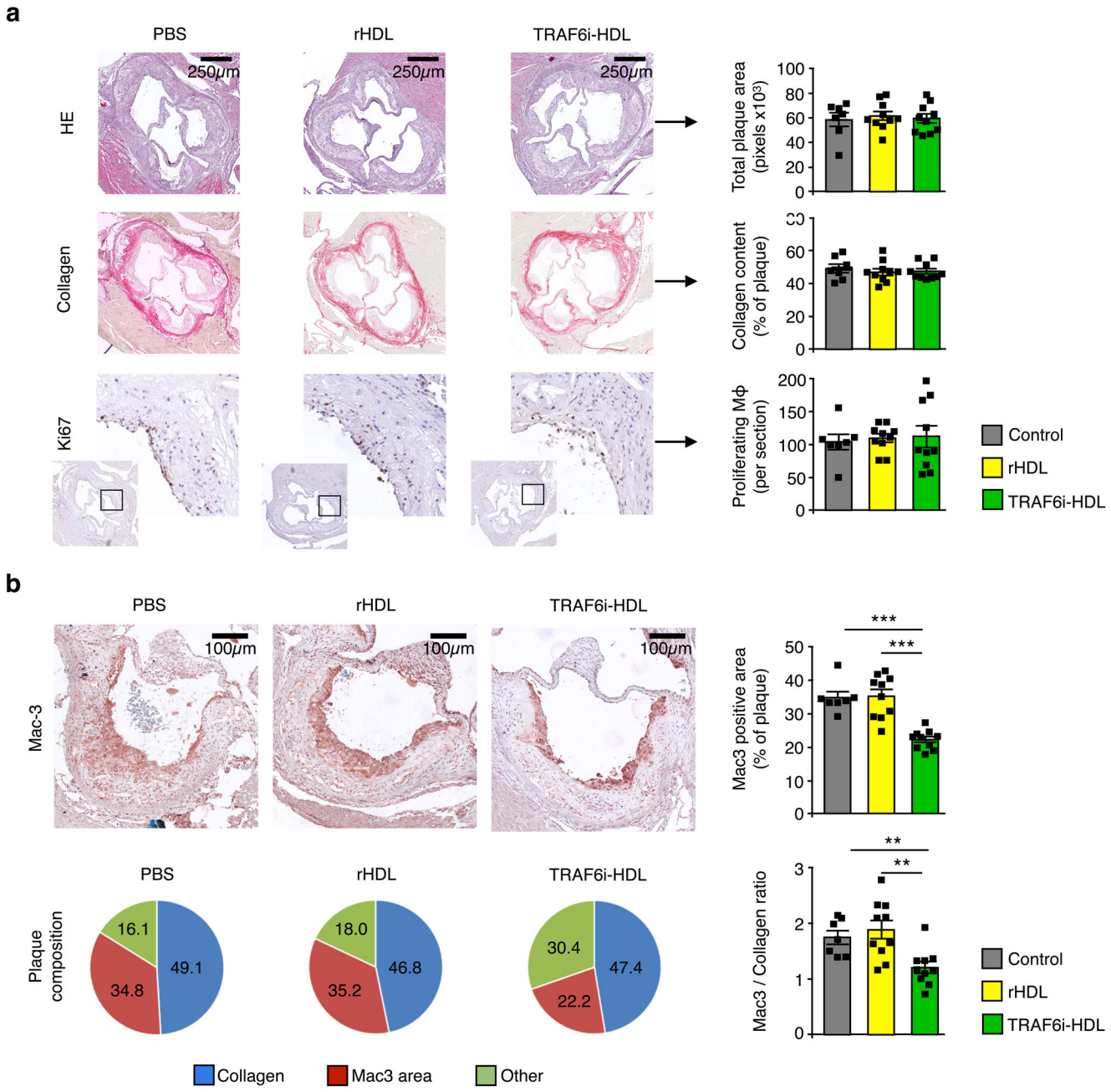


**Figure 3. TRAF6i-HDL therapy decreases plaque macrophage content as assessed by histology.**

Eight-week old Apoe−/− mice were fed a high-cholesterol diet for 12 weeks and subsequently received four intravenous injections of either control (n=10), rHDL (n=10) or TRAF6i-HDL (n=10), over the course of seven days. Twenty-four hours after the last injection, aortic roots were sectioned (4 μM) and stained with (immuno)histochemistry methods. (**a**) Aortic roots show no difference in plaque size (H&E), collagen content (Sirius Red), or number of proliferating cells (Ki67 staining). (**b**) Mac3 staining of aortic roots shows a marked decrease in macrophage positive area in the TRAF6i-HDL group compared to control and rHDL ($p=6.4E^{-4}$ and $p=2.1E^{-4}$ respectively; Kruskal-Wallis $p=1.4E^{-4}$; n=10

per group). The macrophage to collagen ratio was also decreased in the TRAF6i-HDL group compared to control and rHDL ($p=2.5E^{-3}$ and $p=5.2E^{-3}$ respectively; Kruskal-Wallis $p=2.9E^{-3}$; n=10 per group). For all figures: Bars represent the mean and standard error of the mean unless otherwise stated. ** $p < 0.01$, and *** $p < 0.001$. P-values were calculated with Mann-Whitney U tests (two sided).

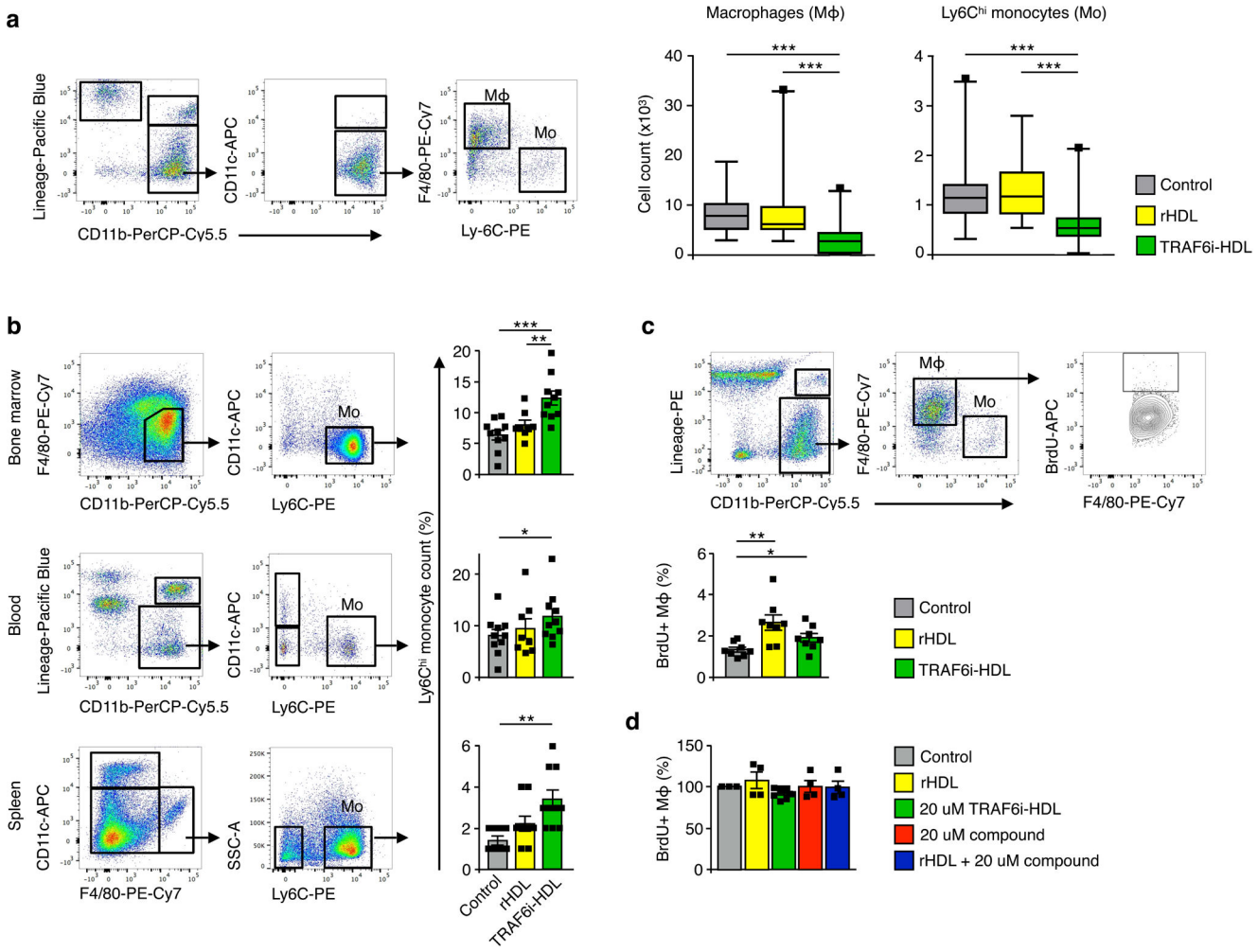


**Figure 4. TRAF6i-HDL decreases plaque inflammation due to impaired Ly6Chi monocyte recruitment.**

Eight-week old Apoe−/− mice on a high-cholesterol diet for 12 weeks and were treated with four intravenous injections of either control (PBS), rHDL or TRAF6i-HDL within a single week. (**a**) Flow cytometry analysis of whole aortas shows a significant reduction in the number of macrophages in the TRAF6i-HDL (n=27) treated group, compared to control (n=27, $p=2.0E^{-6}$) and rHDL (n=26, $p=1.0E^{-5}$, Kruskal-Wallis $p=6.0E^{-7}$). The fact that Ly6C$^{hi}$ monocytes are also markedly reduced in the TRAF6i-HDL group compared to control (n=27, $p=8.9E^{-5}$) and rHDL (n=26, $p=5.6E^{-5}$), indicates impairment of Ly6C$^{hi}$ monocyte recruitment (Kruskal-Wallis $p=2.4E^{-5}$). The box plots indicate the minimum and maximum values (whiskers), the 25th to 75th percentiles (box) and the median (line in the box). (**b**) Flow cytometry analysis of bone marrow, blood and spleen showed that the decrease in plaque Ly6C$^{hi}$ monocyte content could not be attributed to systemic decreases in Ly6C$^{hi}$ monocytes (n=8 to 10 per group, single experiment). In fact, Ly6C$^{hi}$ monocytes were higher in the bone marrow ($p=5.8E^{-4}$), blood ($p=2.7E^{-2}$), and spleen ($p=1.5E^{-3}$) in the TRAF6i-HDL group compared to the control group. There was no significant difference in Ly6C$^{hi}$ monocytes between TRAF6i-HDL and rHDL in the blood (p=0.31) and spleen (p=0.07), while there was a difference between these groups in the bone marrow ($p=5.5E^{-3}$).

(**c**) In vivo BrdU incorporation experiment shows no inhibiting effect of TRAF6i-HDL (n=8) on plaque macrophage proliferation. BrdU incorporation was higher in the rHDL and TRAF6i-HDL group as compared to control ($p=3.3E^{-3}$ and $p=2.7E^{-2}$). (**d**) In vitro experiments (n=3) of BrdU incorporation in RAW 264.7 macrophages treated for 24 hours, with either control, rHDL, TRAF6i-HDL, bare CD40-TRAF6 small molecule inhibitor or a combination of rHDL + bare CD40-TRAF6 small molecule inhibitor, showed no effect on macrophage proliferation.

For all figures means and standard errors of the mean are shown, unless otherwise stated.* $p < 0.05$, ** $p < 0.01$, and *** $p < 0.001$. P-values were calculated with Mann-Whitney U tests (two sided).

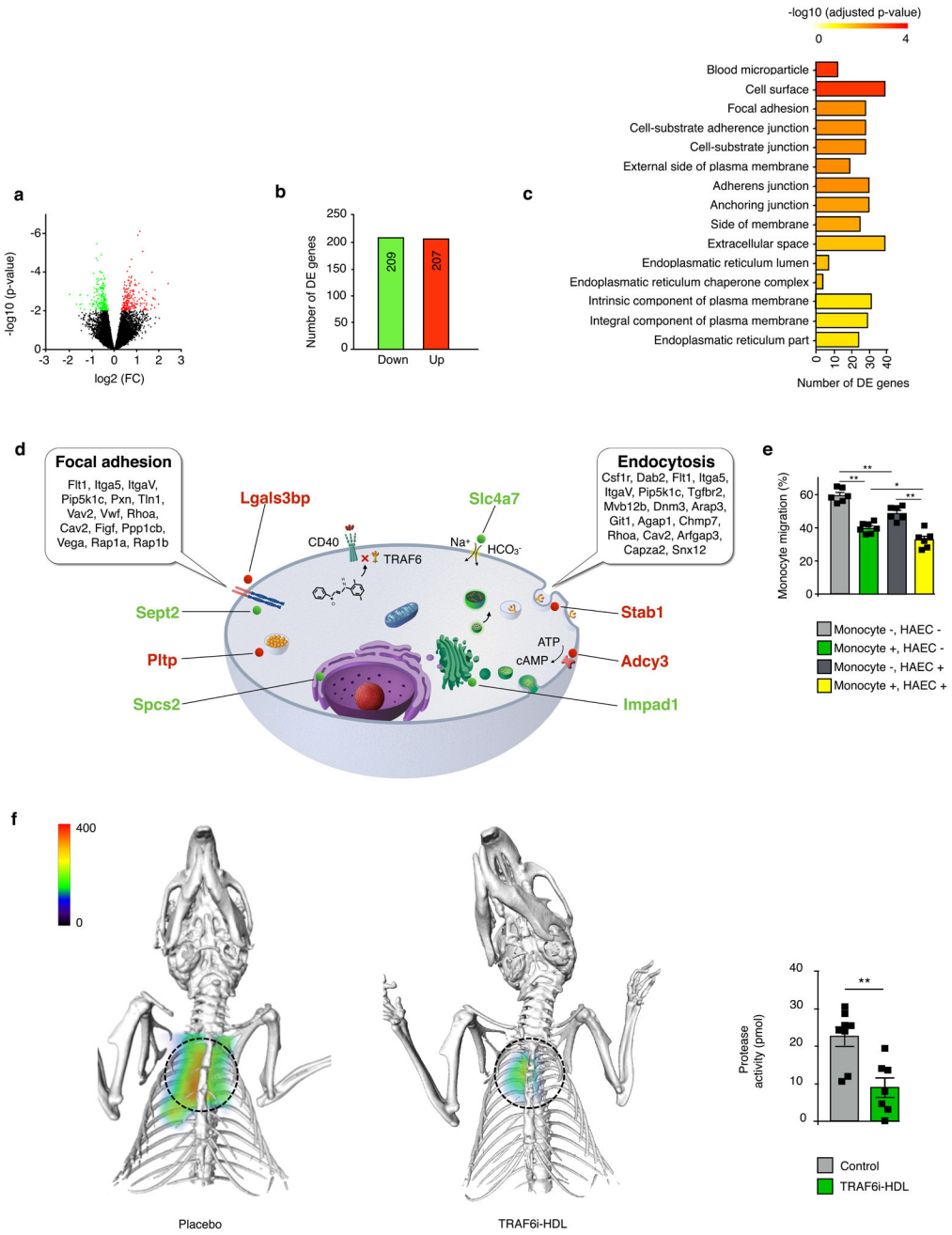


**Figure 5. TRAF6i-HDL shows effects on monocyte migration, among other affected processes.**

(**a to d**) Eight-week old Apoe−/− mice were fed a high-cholesterol diet for 12 weeks and were then treated with four intravenous injections of either control (n=9) or TRAF6i-HDL (n=9) over seven days. Twenty-four hours after the last injection, mice were sacrificed and frozen sections of aortic roots were used for the isolation of plaque macrophages by laser capture microdissection, followed by RNA isolation and sequencing for whole transcriptome analysis. (**a**) Volcano plot, showing the distribution of differentially expressed (DE) genes in plaque monocytes and macrophages. Differential expressed genes between TRAF6i-HDL treatment (n=9) and controls (n=9) were identified using the Bioconductor package limma.

The differentially expressed (DE) genes were identified by a cutoff of an FDR less than 0.2. (**b**) The total number of significantly up- and down-regulated genes, according to cut-off values of an FDR threshold of 0.2. The FDR < 0.2 corresponds to a p-value < 0.009. (**c**) Gene enrichment analysis of the DE gene set within the gene ontology (GO) database, shows 15 GO terms that are significantly enriched with DE genes (Supplementary Table 1). (**d**) Schematic representation of a macrophage showing two significantly altered pathways (focal adhesion and endocytosis) identified by mapping the 416 DE genes with the Kyoto Encyclopedia of Genes and Genomes (KEGG) pathway tool. Also depicted are the 8 most significant DE genes with FDR < 0.05 and their location inside the cell (red is up-regulated, green is down-regulated, Supplementary Table 2 and 3). (**e**) In vitro transendothelial migration assay showing that TRAF6i-HDL inhibits migration of human monocytes over an endothelial barrier (HAECs). P-values for control versus TRAF6i-HDL treated monocytes are $6.2E^{-3}$ (HAEC-) and $1.5E^{-2}$ (HAEC+). In addition to the effect on monocytes, TRAF6i-HDL also has an effect on HAECs, which may contribute to the effect on endothelial transmigration. P-values for control versus TRAF6i-HDL treated endothelial cells are $4.5E^{-3}$ (monocytes-) and $3.9E^{-3}$ (monocytes+). N=6 per treatment condition. + indicates TRAF6i-HDL treated and - indicates control. P-values were calculated with Mann-Whitney U tests (two sided). No adjustment for multiple comparison was made. Bars represent the mean and standard error of the mean. (**f**) FMT/CT imaging shows markedly decreased protease activity in the aortic root in the TRAF6i-HDL (n=7) as compared to the control (n=8) treated group ($P=3.9E^{-3}$). P-values was calculated with Mann-Whitney U tests (two sided). Bars represent the mean and standard error of the mean.

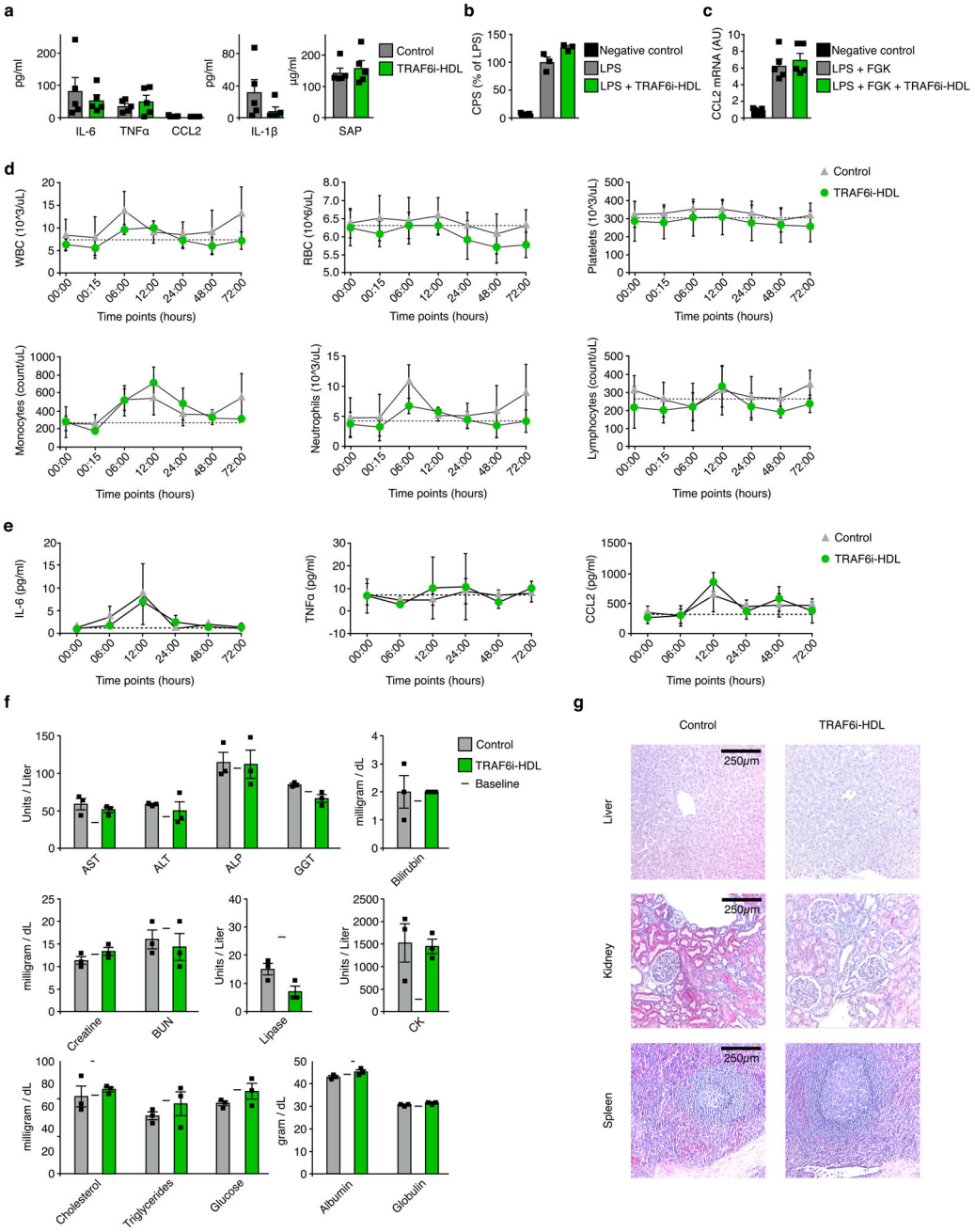


**Figure 6. TRAF6i-HDL therapy shows no adverse immune effects or toxic effects in mice and non-human primates.**

(**a**) Apoe−/− mice were intravenously injected with TRAF6i-HDL at 5 mg/kg or PBS (n=5 per group). Serum was collected 24 hours after injection. We found no signs of systemic immune activation. Interleukin 6 (IL-6), tissue necrosis factor α (TNFα), chemokine (C-C motif) ligand 2 (CCL2), interleukin 1β (IL-1β), and serum amyloid P-component (SAP) levels were not increased. Bars represent means and standard errors of the mean. (**b**) In vitro LPS stimulation test in 3x-κBluc plasmid transfected RAW264.7 cells, showing that TRAF6i-HDL did not affect NFκB activation. Bars represent means and standard errors of

the mean. (**c**) In vitro LPS and FGK45 stimulation test in bone marrow derived macrophages showing that TRAF6i-HDL did not affect CCL2 expression. Bars represent means and standard errors of the mean. (**d to f**) Six non-human primates were infused with either control (n=3) or 1 mg/kg TRAF6i-HDL (n=3). Blood was collected at multiple time points and the animals were sacrificed 72 hours after infusion.(**d**) Complete blood counts showed no effects of TRAF6i-HDL therapy on lymphocytes, erythrocytes and platelets. Means and standard deviations at each timepjoint are shown. (**e**) IL-6, TNFα and CCL2 were not affected by TRAF6i-HDL therapy. Means and standard deviations at each timepjoint are shown. (**f**) Extensive blood chemistry analysis showed no toxic effects of TRAF6i-HDL infusion on hepatic, renal, pancreatic or muscle cell biomarkers. Lipids, glucose, protein (albumin and globulin) and electrolytes were also unaffected. Bars represent means and standard deviations. (**g**) Specimens from liver, kidneys and spleen were sectioned and stained (H&E) for histological analysis and evaluated by a pathologist (10x magnification is shown). No signs of tissue damage or disturbances in tissue architecture were found in any of the tissues (single experiment). For all figures P-values were calculated with Mann-Whitney U tests (two sided). HCT : Hematocrit, MCV : Mean corpuscular volume, MCH : Mean corpuscular hemoglobin, MCHC : Mean corpuscular hemoglobin concentration, HGB : Hemoglobin, ALB : Albumin, GLOB : Globulin, BUN : Blood urea nitrogen, LDH : Lactate dehydrogenase.